

NUREG/CR-3777

SAND84-0912

RV

Printed July 1984

# Capabilities and Diagnostics of the Sandia Pelletron-Raster System

W. H. Buckalew, G. J. Lockwood, S. M. Luker,  
L. E. Ruggles, F. J. Wyant

Prepared by  
Sandia National Laboratories  
Albuquerque, New Mexico 87185 and Livermore, California 94550  
for the United States Department of Energy  
under Contract DE-AC04-76DP00789



Prepared for  
**U. S. NUCLEAR REGULATORY COMMISSION**

#### NOTICE

This report was prepared as an account of work sponsored by an agency of the United States Government. Neither the United States Government nor any agency thereof, or any of their employees, makes any warranty, expressed or implied, or assumes any legal liability or responsibility for any third party's use, or the results of such use, of any information, apparatus product or process disclosed in this report, or represents that its use by such third party would not infringe privately owned rights.

Available from  
GPO Sales Program  
Division of Technical Information and Document Control  
U.S. Nuclear Regulatory Commission  
Washington, D.C. 20555

and  
National Technical Information Service  
Springfield, Virginia 22161

NUREG/CR-3777  
SAND84-0912  
RV

CAPABILITIES AND DIAGNOSTICS OF THE SANDIA  
PELLETRON-RASTER SYSTEM

W. H. Buckalew, G. J. Lockwood, S. M. Luker,  
L. E. Ruggles, F. J. Wyant

Sandia National Laboratories  
Albuquerque, New Mexico 87185  
Operated by  
Sandia Corporation  
for the  
U.S. Department of Energy

Prepared for the Electrical Engineering Branch  
Division of Engineering Technology  
Office of Nuclear Regulatory Research  
U.S. Nuclear Regulatory Commission  
Washington, DC 20555  
Under Interagency Agreement DOE 40-550-75  
NRC FIN No. A-1051

## ABSTRACT

The radiation capabilities of the PELLETRON Electron Beam Accelerator have been expanded to include a controllable, variable dimension, beam diffusion option. This rastered beam option has been studied in detail. Beam characteristics have been determined as a function of incident electron beam energy, current, and deflection system parameters. The beam diagnostics required to define any given diffuse beam pattern are accurate and predictable. Recently, utility of this added PELLETRON capability was demonstrated by simulating the effects of complex nuclear reactor accident electron environments on electrical insulation materials similar to those used in nuclear power plants.

TABLE OF CONTENTS

	Page No.
EXECUTIVE SUMMARY . . . . .	1
1.0 INTRODUCTION . . . . .	2
2.0 APPARATUS AND PROCEDURES . . . . .	3
3.0 RESULTS . . . . .	7
3.1 Beam Characteristics--Vacuum Environment . . . . .	7
3.1.1 Beam Pattern Results . . . . .	7
3.1.2 Beam Dose Results . . . . .	8
3.2 Beam Characteristics--Air Environment . . . . .	9
3.2.1 Beam Transport Through Window Materials . . . . .	9
3.2.2 Beam Transport Through Ambient Air . . . . .	10
4.0 CONCLUSIONS . . . . .	12
REFERENCES . . . . .	13
APPENDIX A . . . . .	14
APPENDIX B . . . . .	17

## LIST OF FIGURES

Figure No.	Page No.
1. Experiment Configuration in Vacuum Environment . . . . .	.20
2. Schematic of the Raster Control System . . . . .	.21
3. Deflector Coil-Target Geometry in Vacuum Chamber . . . . .	.22
4. Experiment Configuration in Air Environment. . . . .	.23
5. Electron Beam Pattern for Equal Deflection Coil Current. . . . .	.24
6. Electron Beam Pattern for Equal Beam Deflection. . . . .	.25
7. Electron Beam Pattern Behind Mask. . . . .	.26
8. Beam Current Partition . . . . .	.27
9. Dosimeter Response Versus Electron Energy. . . . .	.28
10. Dose Versus Stopper Current for 1.0 MeV Electrons. . . . .	.29
11. Beam Deflection as a Function of Coil Current. . . . .	.30
12. Beam Deflection as a Function of Coil Current Frequency. . . . .	.31
13. Beam Deflection as a Function of Electron Energy . . . . .	.32
14. Coil Current Versus Electron Energy. . . . .	.33
15. Dose as a Function of Stopper Current. . . . .	.34
16. Electron Beam Dose Versus Position Following 1.0 MeV Electron Transport Through 0.025-cm Beryllium. . . . .	.35
17. Dose Versus Position . . . . .	.36
18. Electron Beam Pattern for 1.0 MeV Rastered Beam Transport Through 0.0025-cm Mylar Film . . . . .	.37
19. Electron Beam Pattern for 0.4 MeV Rastered Beam Transport Through 0.0025-cm Mylar Film . . . . .	.38
20. Electron Beam Pattern for 1.0 MeV Rastered Beam Transport in Air . . . . .	.39

Figure No.	Page No.
21. Electron Beam Pattern for 0.4 MeV Rastered Beam Transport in Air. . . . .	40
22. (a) Schematic of Deflector Coil-Target Geometry (b) Electron Beam Trajectory in Uniform Magnetic Field . . . . .	41
23. (a) Deflector Coil Dimensions (b) Deflector Coil Wiring Configuration . . . . .	42
24. Coil Current and Driver Voltage as a Function of Time. . . . .	43
25. Magnetic Field Intensity Versus Electron Energy Measured and Calculated Results . . . . .	44
26. Dosimeter Response--Optical Density Versus Absorbed Dose. . . . .	45

LIST OF TABLES

Table No.	Page No.
I. PELLETRON and Raster System Specifications . . . . .	46
II. Beam Current Disposition . . . . .	47
III. Electron Transport in Window Materials . . . . .	48
IV. Electron Transport in Thin Beryllium and Mylar Foils. . . . .	49



## EXECUTIVE SUMMARY

As part of a study on the adequacy of Cobalt-60 sources to simulate the beta component of the radiation field accompanying a nuclear power plant loss-of-coolant accident (LOCA), we have adapted the Sandia PELLETRON\* electron beam accelerator for radiation effects studies on reactor materials and components.

Over the years, the Sandia PELLETRON has been used for physics experiments requiring tightly confined electron beams whose beam energy and current could be tailored on the basis of the individual experiment. In contrast, the LOCA radiation effects studies are best served by diffuse radiation fields. The PELLETRON's variable electron energy capabilities are compatible with those we estimated to be characteristic of many nuclear reactor accident environments. In addition, its beam current capacity is such that large specimens may be exposed to current densities consistent with electron dose rates characteristic of LOCA environments.

Based on the above, we developed a magnetic deflection system capable of generating uniform electron beam patterns of predictable dimension and at current densities and electron energies consistent with those characteristic of nuclear reactor accident electron environments.

The raster system was characterized in terms of accelerator and deflection system parameters by electron beam energy and current, deflection coil current and frequency, and raster pattern size. Characterization was based on electrical measurements and thin film dosimetry which was adapted for this application. Excellent correspondence was obtained between electrical and dosimetry measurements. Sufficient data was obtained to completely define the modified system.

Recently, usefulness of the added PELLETRON capability was demonstrated by studies on the electron beam bombardment of, and charge buildup in, insulation material wherein the mitigating effects of an ambient air environment on charge buildup was demonstrated.\*\*

---

\* Manufactured by National Electrostatics Corporation, Middleton, WI.

\*\* W. H. Buckalew, F. J. Wyant, and G. J. Lockwood, "Response of Rubber Insulation Materials to Monoenergetic Electron Irradiations," SAND83-2098, NUREG/CR-3532, Sandia National Laboratories, November 1983.

## 1.0 INTRODUCTION

The Sandia Laboratories PELLETRON\* electron beam accelerator has been used, over the years, to determine electron number and energy albedos<sup>1</sup>, measure electron energy deposition in material laminates<sup>2</sup>, verify electron transport calculations, and in numerous other research programs. These physics experiments were designed so that a tightly confined steady state electron beam was the appropriate geometry.

For some time there has existed the need to determine the adequacy of isotopic photon irradiators to simulate electron effects, peculiar to nuclear reactor accident electron environments, on exposed organic materials and components<sup>3</sup>. These accident radiation environments are complex<sup>4</sup> in that both the electron energy spectrum and energy deposition rate are time dependent. However, these spectra and deposition rates may be categorized on the basis of several discrete average particle energies and energy deposition rates. In general, radiation effects experiments involving reactor materials and components are best served by diffuse radiation fields.

The PELLETRON electron beam generator possesses the variable electron energy capabilities that span the average electron energies estimated to be characteristic of many nuclear reactor accident (electron) environments<sup>3</sup>. Further, its beam current capacity is such that large specimens could be exposed to current densities consistent with electron dose rates that are characteristic of reactor accident environments.

Based on the reactor accident electron environment and the capabilities of the PELLETRON, we developed (and modified the accelerator with) a magnetic deflection system capable of generating uniform electron patterns of predictable dimensions and at current densities and electron energies consistent with those characteristic of nuclear reactor accident electron environments. Table I lists the pertinent parameters of the PELLETRON/Raster system as it now exists.

As a diagnostic aid for characterizing the deflection system, we adapted available thin film dosimetry material for beam pattern and absorbed dose diagnostics. In addition, with the aid of electron beam transport calculations, we established correspondence between electron beam dose measured with thin film dosimetry and those estimated on the basis of observed electron beam currents.

---

\* Manufactured by National Electrostatics Corporation, Middleton, WI.

As a result of this investigation, the PELLETRON has been adapted to provide predictable diffuse electron beams suitable for electron effect studies on material samples of (relatively) large cross-sectional area. Recently the utility of this refinement was demonstrated during a successful investigation of the charge deposition in insulating material undergoing electron beam bombardment<sup>5</sup>.

## 2.0 APPARATUS AND PROCEDURES

The beam deflection system capabilities were characterized for both vacuum and ambient air environments. Vacuum environments were obtained in the PELLETRON accelerator's 1.2-meter (diameter) vacuum chamber. The generous dimensions of the chamber allowed complete definition of the deflection system. Ambient air measurements by comparison were modest. System performance in the vacuum environment was characterized first for several reasons, the most important being the absence of (1) electron beam energy degradation, and (2) collision-generated secondary currents.

Figure 1 is a schematic of the components essential to the "in vacuum" system characterization. The primary elements are a Faraday Cup, beam deflector, target assembly, and beryllium-aluminum (Be-Al) stopper plate. Component functions are as follows.

The Faraday Cup, enabled by closure of the movable end plate, serves to measure the total accelerator beam current. Faraday Cup current is an indicator of machine performance and is the primary aid in adjusting accelerator output for the dose rate selected. Rigidly attached in line to the Faraday Cup are the four magnetic deflection (raster) system coils.

The deflection control system, depicted by the schematic presented in Figure 2, consists of two identical drive units. Elements comprising each drive unit are a wave function generator, current source, and a pair of deflection coils. The deflection coils are attached (on opposing surfaces) to an aluminum drift tube, 12-cm long and 2.6-cm in diameter. Orientation of each pair of coils is either in the horizontal or vertical plane; e.g., the horizontal deflection coils are oriented in the vertical plane. The coils are connected, electrically, in series and with coil windings in phase so that each pair of coils represents a single, pseudo infinite (long) coil, positioned along the drift tube axial centerline. Current to each pair of coils is supplied by a bipolar current source with a four ampere (peak) capacity. Current wave form and frequency output, from the current source, is controlled by a

variable function generator. An oscilloscope placed across the current viewing resistor, which is in series with the coil current source and signal generator, monitors the current and current frequency input to the deflection coils. In order to generate an almost linear electron sweep, a triangular wave form is input to the current source. By maintaining a frequency difference between the two drive units, beam pattern retrace effects are minimized. Additional details of the deflection system are given in Appendix A.

In alignment with, and positioned behind the deflection coils is the target assembly. The assembly consists of a mask, a target holder, and a beam stopper. The mask is an aluminum slab, infinitely thick to the most energetic electrons. An orifice, with dimensions determined by the experiment, is centrally located in the mask. The mask is electrically insulated and monitored with a high sensitivity current detector (electrometer). In practice, the mask orifice is always smaller than the deflected beam pattern so that the effects of coil inductance on the electron beam intensity near the pattern periphery are screened from the experiment. The intercepted component of the beam is accounted for by the mask current detector. The use of a mask assures that a spatially uniform beam will be incident on the test specimen.

The target holder is an aluminum clamping device in which the sample to be irradiated is positioned. The holder is electrically insulated and may be monitored with an electrometer, if required. The holder is also adjustable so that sample thickness may range from 0.002-cm to >1.3-cm.

The final element in the experimental array is the beryllium aluminum (Be-Al) stopper. This element consists of a (current) monitored laminate of beryllium and aluminum. The element is also infinitely thick to the most energetic electrons so that the total current transmitted by the mask is detected. Since the stopper is placed in close proximity to the mask element, detection of current incident on the stopper allows for an independent determination of exposure dose rate in the target zone between the mask and stopper elements. Presence of the beryllium lamina on the stopper assures minimized electron backscatter into the target volume.

Using the configuration depicted in Figure 1, we systematically characterized the raster system capabilities on the basis of electron beam energy, raster coil current, and current frequency. Since beam pattern dimensions are position dependent, target-raster coil separation distances were held constant. Separation distances used are those shown on the schematic presented in Figure 3. Depending on the application, the

target/dosimetry plane designation, in Figure 3, may be considered as either the mask or stopper element, or anywhere between the two.

The configuration for ambient air diagnostics is shown in Figure 4. Except for the inclusion of an additional mask and a thin film window interface, mounted in the vacuum chamber flange, the configuration is similar to that used for the "in vacuum" diagnostics. From Figure 4 we note that the vacuum mask is placed near the flange interface so that alignment of the electron beam is easily determined. An instrumented mask and beam stopper are mounted in close proximity to the flange exit. Ambient air diagnostics were obtained on the mask and in the region between the mask and stopper elements. Due to the placement of the deflection coils with respect to the flange window, beam pattern size is severely limited, and the amount of ambient air diagnostics to date is quite modest. It is anticipated that the deflection system will be attached to the flange and more extensive diagnostics will be obtained in the future. To date, most ambient measurements are for electron beam patterns on the order of 2.5-cm (diameter). However, rather extensive data have been obtained on the effects of window material and material thickness on electron beam transport.

Rastered beam diagnostics were obtained with thin film dosimetry and determination of the electron beam current disposition. Electron beam dimensions and uniformity were obtained with a radiation sensitive thin film material. Since the film dimensions are 15-cm by 15-cm by 0.005-cm thick, large beam patterns may be measured with minimum perturbation to the incident electron beam energy. Prior to use, the dosimetry material was calibrated in the Sandia gamma irradiation facility (GIF). The calibration linked foil optical density with absorbed radiation dose. We observed that film response, monitored with a scanning microdensitometer, was linear with absorbed radiation dose. Details of the calibration methods are given in Appendix B. For vacuum measurements (Figure 1) dosimetry film was placed on the mask front surface and usually on the mask back surface or in the target region between the mask and stopper elements. Regardless of location, the dosimetry material was oriented so that its horizontal and vertical axes were parallel to the corresponding mask axes. Following irradiation, each dosimeter foil was optically scanned along both its horizontal and vertical centerline axes. Measurements thus obtained from film placed on the mask front surface yielded data on electron beam pattern size and uniformity as a function of the several accelerator and deflection coil parameters. Figure 5 presents typical unconverted dosimetry data obtained from film placed on the mask front surface. Optical density is plotted as a function of

relative position along the film's vertical and horizontal centerlines. Beam energy was 1.0 MeV, coil current was 1.5 amperes, and current frequency was 100 Hz for the horizontal deflector coils and 33 Hz for the vertical deflector coils. The increase in optical density near the edge of each traverse may be attributed to deflector coil inductance. Note also the increase in beam pattern nonuniformity at the higher coil frequency. In Figures 6 and 7, mask effects on beam uniformity are illustrated. These figures are based on data obtained from simultaneous exposure of dosimetry foils placed on the front and back surface of the mask element. The front surface data, Figure 6, is similar to that presented in Figure 5. The large spike appearing on each trace was caused by an un rastered beam exposure that was used as a check on the alignment of the mask, foil, and stopper. Other, smaller spikes are the result of scratches, dust, etc. on the foil surface. In Figure 7 we note the mask has eliminated all nonuniformities caused by the deflector coil inductances.

Concurrent with thin film dosimetry measurements, complete beam current measurements were obtained, i.e., Faraday Cup, mask, and stopper currents were monitored. For all "in vacuum" measurements, we were able to account for the total current disposition. Typical current partition data is presented in Figure 8 and Table II. This data was obtained at an electron beam energy of 1.0 MeV. The horizontal coil current was 1.34 amperes (peak-to-peak) and the vertical coil current was 1.67 amperes. Coil current frequencies were 33 Hz and 100 Hz, respectively. In the figure, mask and stopper currents are plotted as a function of the Faraday Cup current. As may be observed, measured stopper and mask current track linearly with the observed Faraday Cup current. Current conservation is demonstrated by the data tabulation given in Table II where unaccounted for current losses are never greater than four percent. It should be noted that the mask and stopper data have been adjusted to account for electron reflection (backscatter) losses. The adjustments were based on experimentally determined albedos reported in Reference 1. These electrical measurements can be directly linked to thin film dosimetry results through the stopper current determinations. Thin film dosimetry placed behind the mask, in the region between the mask and stopper, intercepts the same total current detected by the stopper element. Figure 9 is a plot of measured dosimeter response, MeV/gm per  $e^-/\text{cm}^2$  incident, as a function of electron energy. Dosimetry results were normalized on the basis of observed stopper current and mask orifice dimensions; i.e., normalized on the basis of one electron per square centimeter. Plotted also on the figure is calculated dosimeter response. Calculated values were obtained with the coupled electron-photon transport code, TIGER<sup>6</sup>. Plotted in Figure 10 are some dose estimates based

on thin film dosimetry (measured) and stopper currents (calculated). Data for this plot was obtained at an electron beam energy of 1.0 MeV. The measured dose estimates were derived from film exposed concurrent with the electrical measurements appearing in Table II. Calculated results were obtained from the observed stopper currents (listed in Table II) and the film response coefficients calculated with the TIGER code. Similar results were obtained for other electron energies. The fall-off of film response, at the high current, was attributed to oxygen depletion in the dosimetry material. The measured-adjusted data point was based on an experimentally determined correction factor for oxygen depletion. On the basis of the presented (and other) data, stopper current and thin film data may be used interchangeably. In addition, since correspondence was established between Faraday Cup, mask, and stopper currents, the Faraday Cup may be used to estimate beam current required to deliver a given dose rate into the target zone.

Diagnostic techniques for ambient air environments were similar to those used in the "in vacuum" measurements.

### 3.0 RESULTS

#### 3.1 Beam Characteristics--Vacuum Environment

##### 3.1.1 Beam Pattern Results

The rastered PELLETRON electron beam was systematically investigated as a function of beam energy, deflection coil current, and current frequency. Recall, Figure 3, that the target-deflector coil separation for these measurements was 70 centimeters. All of the beam uniformity and pattern size data were obtained using thin film dosimetry. Dose determinations were based on either foil or stopper current measurements. The preponderance of these data were obtained for a one MeV beam energy and for coil frequencies of 33 and 100 Hz. Sufficient data was obtained at other beam energies and frequencies so that trends at those energies and frequencies could be established. It was observed that beam pattern size was maximized and the effects of coil inductance was minimized with decreasing coil drive frequency. However, for frequencies less than 30 Hz we noted a marked "woven" pattern in the dosimetry foil optical density. We attributed this to beam retrace.

The deflected beam pattern results are summarized in Figures 11, 12, 13, and 14. In Figure 11 beam deflection as a function of coil current is depicted for current drive frequency maintained constant at 33 Hz (left-hand figure) and 100 Hz (right-hand figure) respectively. These data sets were acquired simultaneously by driving one set of deflection coils at 33 Hz and the other pair at 100 Hz. Electron beam energies for each frequency were 0.2, 0.4, 0.6, 0.8, and 1.0 MeV. We note that the beam deflection is reasonably linear with deflector coil current. The strong dependence of beam deflection on beam energy is evident for both drive frequencies, however beam deflection dependency on drive frequency is much more subtle. Beam deflection as a function of current frequency, for coil current fixed at 1.5 amperes peak, is depicted in Figure 12. For frequencies in the range of 30 to 250 Hz and 1.0 MeV electron beam energy, we note a linear relationship between beam deflection and coil current frequency. Although data for the other beam energies is confined to 33 and 100 Hz, based on the 1.0 MeV beam behavior, we infer deflection response to the other coil frequencies should follow the trends observed for the one MeV beam. Figure 13 is a plot of electron beam deflection response to beam energy and coil drive frequency. In the plot, peak coil current is fixed at 1.0 ampere and drive frequency is limited to 33 and 100 Hz. Again, the strong dependence of beam deflection on electron beam energy is evident as is the mild response of beam deflection to current drive frequency. Coil current is plotted as a function of electron beam energy for fixed deflection and coil frequencies of 33 and 100 Hz in Figure 14.

The data presented in Figures 11, 12, 13, and 14 completely define the raster system in terms of all pertinent parameters (i.e., electron energy, coil current, drive frequency, and beam deflection). System behavior is sufficiently regular so that any other set of conditions may be obtained, within the original experimental limits, from the data presented in these four figures.

### 3.1.2 Beam Dose Results

Dose measurements, for several electron beam energies, were obtained as a function of measured stopper current which is linearly related to both the Faraday Cup and mask currents. These data were obtained while keeping the time of irradiation constant. The dose values were measured with the thin film dosimetry placed in the target zone between the mask and stopper elements. In addition, dose estimates were based on measured stopper currents and calculated energy absorption coefficients (from the transport code TIGER). Figure 15 is a plot of these



results. Dose as a function of stopper current is plotted for electron beam energies in the energy range of 0.2 to 1.0 MeV. For each curve, the dose data are a composite (simple average) of the dose estimates obtained by the two methods described above (i.e., thin film and stopper current techniques).

### 3.2 Beam Characteristics--Ambient Air Environment

#### 3.2.1 Beam Transport Through Window Materials

Prior to extracting the electron beam into an ambient air environment, preliminary measurements and calculations were obtained on the perturbing effects of several window materials on the transported electron beam. Window materials considered were those readily available and consisted of thin mylar film and beryllium foil. Thickness of the mylar film was in the range of 0.0025 cm. The beryllium foil, fitted into a holder compatible with the PELLETRON exit flange, was 0.0254 cm thick. These experiments were performed in a vacuum environment using the experiment configuration depicted in Figure 1. The 0.0025 cm Mylar film and 0.0254 cm beryllium foil were evaluated. The window materials were placed on the mask back surface and the dosimetry material was attached to the stopper element positioned 4.1 cm behind the mask. Using an unrastered beam, we examined the transport properties of both the beryllium foil and mylar film as window materials.

In Figure 16 the effect of beryllium on the transport of 1 MeV electrons is shown. The plot shows the thin film dosimeter response (absorbed dose) to the transported beam as a function of position in the target plane normal to the incident beam. Based on the beryllium-dosimeter separation distance, and a tightly confined incident beam, the electron beam is scattered into an angle of  $\sim 40^\circ$ . Calculations of 1 MeV electron transport through 0.0254 cm beryllium slabs predict a scattering angle of  $30^\circ$  contains  $\sim 90$  percent of the incident beam and that average energy of the transmitted beam is approximately 0.9 MeV.

Using the electron transport data and calculated electron fluence-to-dose conversion factors, we constructed a histogram dose profile for a 4.1 cm target-detector separation. These histogram data have been superimposed on the measured dose profile. As may be observed, the calculated histogram which is normalized to the measured results on the basis of the observed stopper current is in good agreement with the measured dose profile.

Similar measurements and calculations were obtained for 1.0 and 0.4 MeV electron transport in mylar films. These data and calculations predict that for tightly confined 1 MeV electrons incident on 0.00254 cm mylar film, the scattering angle is approximately  $15^\circ$ . Average energy of the transmitted beam is about equal to the incident beam energy. For 0.4 MeV electrons, the transmitted beam was markedly more diffuse. Approximately 0.99 of the incident beam was confined to an angle of  $\sim 25^\circ$ . Again incident beam energy degradation was of minor significance. In Figure 17 we have plotted the calculated results--absorbed dose as a function of position in the dose plane separated 4.1-cm from the mylar window. The calculated results have been normalized on the basis of observed stopper currents. Table III gives the calculated results for the transport of both 0.4 and 1.0 MeV electrons through the mylar and beryllium window materials. Listed in the tabulation are transmitted electron fraction as a function of scattering angle. Based on these measurements and calculations for the two materials, mylar was the preferred window material from the standpoint of beam transport. In practice, it was observed that continuous electron bombardment of the mylar window caused material embrittlement and resulted in subsequent window rupture. Because of the fragile nature of the mylar film, we investigated (analytically) further the transport properties of thin beryllium foil. For comparable thicknesses of beryllium and mylar, beryllium possesses as good or better transmission properties than mylar. Based on this investigation, we are fabricating prototype 0.00508 cm beryllium windows for use in future simulation studies. A tabulation of the transport properties of comparable thicknesses of beryllium and mylar windows is given in Table IV.

Window effects on transport of a 1.0 MeV rastered beam through a 0.00254 cm mylar window are shown in Figure 18. We have plotted optical density as a function of position along the (film's) vertical and horizontal axes. The rastered beam was incident on a mask with a 2.54 cm (diameter) orifice, and the dosimetry film was again placed 4.1 cm behind the mask orifice. We note some broadening of the transmitted beam consistent with the unrastered beam results. Figure 19 presents rastered beam transmission data for 0.4 MeV beam energy. We note that beam spreading for the 0.4 MeV beam is somewhat more pronounced than for the 1.0 MeV case.

### 3.2.2 Beam Characteristics--Ambient Air

Rastered beam characteristics, in ambient air, were obtained for both 1.0 and 0.4 MeV beam energies. The diagnostics consisted of thin film dosimetry and beam current measurements.

The experimental configuration appearing in Figure 4 was used to obtain the ambient air data. The rastered electron beam was transported, in vacuum, to mask-1 where it was collimated to a 2.54 cm diameter circular pattern. Since the collimated beam dimension was less than the exit flange window dimension, beam scatter during transport through the vacuum chamber was minimized. Upon exit into ambient air, the beam was again collimated prior to transport into the target region. Finally, the beam was terminated in the stopper element.

For air transport, the beam dose distribution was monitored on exit from mask-2 and again in the target region. Separation between mask-2 and the mylar window was 4.6 cm and between mask 2 and the film holder, in the target region, the separation was 1.3 cm. Distance between the film holder and the stopper was 1.0 cm.

Diagnostics consisted of thin film dosimetry and stopper current measurements. The thin film dosimetry data for 1.0 MeV electron transport in air is shown in Figure 20. All traces were obtained from densitometer scans along the vertical centerlines. The left-hand trace was obtained from film located in the target holder and the other from film located on the mask-2 rear surface. We note very little beam divergence as the beam is transported from the mask to the film holder, and beam attenuation is insignificant. Figure 21 depicts comparable data for the 0.4 MeV electron beam. Again the left-hand trace was obtained at the sample holder and the right-hand trace at the mask-2 rear surface. We observe some beam nonuniformities at the mask-2 exit and a measurable beam attenuation as it progresses to the target region film retainer. This observation is consistent with the expectation that stopping power increases as electron energy decreases.

Correlation between film and stopper current dose determinations were excellent. For 1.0 MeV irradiations the film predicted a dose of 1.25 Mrad and the stopper current estimate was 1.24 Mrad. At 0.4 MeV the film measured 2.4 Mrad and the stopper current predicted 2.45 Mrad. The Faraday Cup current during these irradiations was 2.0 microamperes for the 1.0 MeV exposure and 3.75 microamperes for the 0.4 MeV run. Each irradiation time was 300 seconds, hence we achieved dose rates in the range of 10 to 25 Mrads/hr, and the capability exists to significantly increase those exposure rates by increasing beam current.

#### 4.0 CONCLUSIONS

The PELLETRON is a high stability, well characterized, variable voltage, variable current electron beam generator originally designed to deliver tight collimated electron beams into target areas. The machine's radiation effects capabilities have been significantly enhanced by the addition of a beam scanning/deflector (raster) system that permits deflection of the electron beam into large uniform patterns. The scanning system behavior was extensively studied in both vacuum and air environments. Deflected electron beam dimensions and uniformity were characterized as a function of all scanning system parameters. Correlation between deflection coil current, current frequency, and electron beam energy as a function of beam dimensions and uniformity were established. Further, correspondence between measured absorbed dose and electron beam current was demonstrated.

In the PELLETRON internal vacuum chamber, the deflected electron beam dimensions may be varied over a wide range. Rectangular patterns with dimensions between 2.5 and 15 cm are readily attainable. Depending on pattern dimensions and electron beam energy, absorbed dose rate is variable between 0.1 and 30 Mrad/hr. Because of the exit flange size, dimensions of the beam extracted external to the vacuum chamber and into the ambient air environment is currently restricted to 2.5 cm (diameter). Dose rates in air have been measured and are comparable to those attainable in vacuum. For future ambient air experiments, it is planned to position the deflection coils adjacent to the exit flange. With this configuration beam dimensions comparable to those obtained in vacuum will be achievable.

Utility of the PELLETRON's enhanced capabilities was recently demonstrated. Electron radiation fields accompanying a postulated nuclear power plant loss of coolant accident were simulated for radiation effects studies on power plant cable insulation materials<sup>5</sup>. It was demonstrated that both electron dose/dose rates and electron energy spectra were adequately simulated with such large diffuse monoenergetic beams.

## REFERENCES

1. G. J. Lockwood, L. E. Ruggles, G. H. Miller, and J. A. Halbleib, "Electron Energy and Charge Albedos--Calorimetric Measurements vs Monte-Carlo Theory," SAND80-1968, Sandia National Laboratories, November 1981.
2. G. J. Lockwood, L. E. Ruggles, G. H. Miller, and J. A. Halbleib, "Calorimetric Measurements of Electron Energy Deposition in Extended Media--Theory vs Experiment," SAND79 0414, Sandia National Laboratories, January, 1980.
3. L. L. Bonzon and W. H. Buckalew, "Evaluation of Simulator Adequacy for the Radiation Qualification of Safety Related Equipment," SAND79-1787, NUREG/CR-1184, Sandia National Laboratories, January 1980.
4. L. L. Bonzon et al., "An Overview of Equipment Survivability Studies at Sandia National Laboratories (SNL)," SAND83 0759C, Sandia National Laboratories, Presented at the International Meeting on Light-Water Reactor Severe Accident Evaluation Conference, Cambridge, MA, August 28-September 1, 1983.
5. W. H. Buckalew, F. J. Wyant, and G. J. Lockwood, "Response of Rubber Insulation Materials to Monoenergetic Electron Irradiations," SAND83-2098, NUREG/CR-3532, Sandia National Laboratories, November 1983.
6. J. A. Halbleib, Jr. and W. H. Vandevender, Nucl. Sci. Eng., 57, 94(1975).

## APPENDIX A

### Raster Design Considerations

Many PELLETRON applications are best served by a tightly confined electron beam\*. However, simulation of LOCA electron radiation environments requires large diffuse beam geometries. The beam deflection system (raster) was primarily based on space considerations within the PELLETRON vacuum chamber. Maximum target-deflector separation in the 1.2 meter diameter chamber is approximately 85 cm and an upper practical limit on sample dimension is on the order of 15 cm. In Figure 22-a is presented a schematic of the deflector-target orientation within the vacuum chamber. D is the target-deflector separation and h is one half the target maximum lateral dimension.

Using these maximum physical separation dimensions, we calculated the magnetic field required to deflect 1.0 MeV electrons sufficiently to span the target area. The relationship describing the trajectory of an electron traversing a uniform magnetic field is:

$$\frac{mv}{R} = Be = e\mu H$$

where, R is the radius of curvature of the deflected electron,  
B is the magnetic flux density,  
H is the magnetic field intensity,  
 $\mu$  is the permeability of the medium,  
e is the charge on the electron,  
m is the electron mass, and  
v is the electron velocity.

Figure 22-b depicts the relationship between the electron radius of curvature (R), deflector-target separation (D), electron flight path ( $\ell$ ), target dimension (h), and deflector coil (drift tube) dimension (2s). Based on geometric considerations, it can be shown that the electron radius of curvature is related to the dimensions within the vacuum tank as:

$$R = \frac{(\ell + D)r}{h}$$

where, r is  $R \tan \frac{(\theta)}{2}$ .

\*G. J. Lockwood, L. E. Ruggles, G. H. Miller, and J. A. Haibleib, "Calorimetric Measurements of Electron Energy Deposition in Extended Media--Theory vs Experiment," SAND79 0410, Sandia National Laboratories, January 1980.

Since all deflection angles are small, R is, to a good approximation:

$$R \approx \frac{2rD}{h} \approx \frac{2sD}{h}$$

Having obtained the required radius of curvature, we estimate the magnetic field intensity to be:

$$H = \frac{mv}{e\mu R} = \frac{m_0 v}{e\mu R} \frac{v}{c} \left[ 1 - \left( \frac{v}{c} \right)^2 \right]^{-\frac{1}{2}}$$

$$= 3500 \text{ ampere-turns/meter}$$

where the electron mass, m, has now been replaced by its rest mass,  $m_0$ .

This estimate of required magnetic field intensity is based on the field intensity in the center of an infinite length coil; i.e., no edge effects.

Our beam deflection (raster) system consists of a 12-cm long aluminum drift tube with a 2.2-cm diameter cylindrical void. Attached to the drift tube, concurrent to its axial centerline, are four deflection coils spaced radially at 90 degrees about its axis. Each coil consists of 400 turns of #20 varnished magnet wire wound on an aluminum coil form 9-cm long by 1.27-cm wide by 5.1-cm high. The coil density for each deflector unit is 7840 turns/meter. Figure 23-a shows the drift tube coil form configuration. The coil and drift tube assembly is mounted on the Faraday Cup back surface flange so that one pair of coils lies in the horizontal plane and the other in the vertical plane. Coils in each plane are electrically connected in an in phase, in-series arrangement. In Figure 23-b is shown the wiring configuration for a pair of deflection coils.

Each pair of coils is powered by a 4 ampere (peak) variable frequency, variable current, bipolar, current supply. In normal operation, we limited coil current to 2 amperes or less. To assure a uniform diffuse beam pattern, a coil frequency difference between each set of coils was maintained. In order to assure linear electron deflection and hence a uniform irradiation, a triangular current waveform was used to drive the deflection coils. Figure 24 presents calculated coil current and driver voltage as a function of time. We note an almost linear coil current waveform with some distortion (roll-over) as the driver voltage slope is reversed. Current roll-over manifests itself as dose enhancement at the region of roll-over on the target material.

The solution to the electron trajectory equation predicts a magnetic field intensity of 3300 ampere-turns/meter would be required to achieve the maximum electron deflection under ideal conditions; i.e., in the center of an infinite coil. However, the infinite coil requirement is not attainable and, in fact, in the vicinity of the drift tube, field uniformity is probably not good. We compensate for this with a high winding density. For maximum deflection, we have:

$$H = (7840 \text{ turns/meter})(2.0 \text{ amperes}) = 15680 \text{ ampere-turns/meter}$$

Thus we have a deflection unit over-designed by about a factor of five (greater than theoretical) to account for nonuniformity of the field in the vicinity of the drift tube and coil inductive effects on scanning linearity. In Figure 25 is presented the calculated and some measured magnetic field intensities required for a constant beam deflection versus electron energy. We note that at 33 hz actual versus calculated field intensity is almost a factor of 5 different; however, as drive frequency is increased, coil current requirements also increase. In order to minimize coil current requirements, drive frequencies should be kept as low as possible, consistent with minimized scan retrace effects.



## APPENDIX B

### Electron Beam Dose Diagnostics Considerations

Diagnostics of the rastered electron beam requires gaining knowledge of the beam uniformity and intensity in terms of absorbed dose and dose rate as a function of the parameters beam energy, beam deflector current, deflector current frequency, etc. Several dosimetry systems are available for beam dose/dose rate diagnostics. Systems include both active and passive detectors. Examples of active detectors are photodiodes and instrumented carbon blocks. Thermoluminescent detector (TLD) chips, activated glass, and dye-loaded film are representative of passive detectors. The major drawback of many of these systems for our application is that they are pseudo-point detectors. This implies that spatial beam diagnostics, of diffuse beams, will have limited spatial resolution. In addition, use of large numbers of detectors complicates bookkeeping and requires a great amount of careful detector positioning for each diagnostic measurement. Other drawbacks may include beam perturbation by the detector, one time readout capability, low to moderate integrated dose range, etc.

In view of the above, we chose to base beam diagnostics on thin film dosimetry\*. Thin film dosimetry offers minimized beam perturbation, non-destructive readout, high integrated dose capability, large cross-section area, and (depending on readout or scanning technique) excellent spatial resolution. The dosimetry system chosen consisted of nylon and polychlorostyrene films available in 15 by 15 cm squares, 0.00508 cm thick.

Thin film dosimeter response to ionizing radiation is determined by observing the growth of either absorption or transmission peaks at specific wavelengths in the visible spectrum and establishing the relationship between absorbed dose and light absorption/transmission properties of the irradiated film. To be useful, thin film optical response should be reasonably linear with absorbed dose.

We calibrated film response to ionizing radiation on a Cobalt-60 source range\*\*. Gamma dose rates at several locations in the irradiation cell were determined with an NBS traceable Victoreen 550 Radacon III integrating rate meter and type 550-6 air ionization probe. Calibration samples of nylon and polychlorostyrene film, 3.8 cm square, were exposed in air at the

---

\*Farwest Technology Inc., Goleta, CA.

\*\*Gamma Irradiation Facility (GIF) at Sandia National Laboratories, Albuquerque, NM.

calibrated locations to integrated doses in the range of 0.1 to 10 Mrad (air). For each exposure, positions were selected so that exposure time would not introduce a significant uncertainty. For all exposures, the dosimetry samples were enclosed in 0.378 g/cm<sup>2</sup> lucite electron equilibrators, thus assuring that a state of electron equilibrium would be established.

We assume that irradiated film response is proportional to the incident photon energy fluence and that the energy deposited per unit thickness of dosimeter,  $D$ , is given by:

$$D = f\mu_a E$$

where,  $f$  is the fraction of energy deposited that is retained,  $\mu_a$  is the energy absorption coefficient, and  $E$  is the incident energy flux.

For an equilibrated detector film,  $f$  effectively approaches a value of 1, in that recoils escaping the foil back surface are exactly balanced by those entering the front surface. The number of absorption centers ( $N$ ) created per unit foil thickness is then:

$$N = D\alpha n$$

where,  $\alpha$  is the number of absorption center precursors activated per unit energy absorbed, and  $n$  is the composite absorption center precursor; i.e., dye concentration, oxygen concentration, etc. (number/g).

Provided no depletion of precursors occurs, growth of absorption peaks in the irradiated film should be linear with absorbed dose. Change in light intensity ( $dI$ ), at wavelength  $\lambda$ , per unit distance ( $dx$ ) in the irradiated film is:

$$-\frac{dI}{dx} = IN$$

and, solving for  $I$ :

$$I = I_0 \exp(-Nx)$$

where,  $I_0$ ,  $I$  are the incident and transmitted light intensity of wavelength  $\lambda$ , and  $x$  is the film thickness.

Irradiated film is read with a scanning microdensitometer. Light transmitted through the irradiated film is passed through interference filters so that film response to a narrow band of frequencies is measured. The microdensitometer output consists of optical density versus position plots. Since optical density (OD) is defined as:

$$OD = \log \left( \frac{I_0}{I} \right)$$

we note that the microdensitometer output, optical density versus position, gives a plot linearly proportional to dose, since:

$$OD = \log \left( \frac{I_0}{I} \right) = Nx = \alpha n f \mu_a x E$$

where we recall that  $f \mu_a E$  was defined as the absorbed incident photon energy flux. In Figure 26 is presented calibration data obtained from chlorostyrene films irradiated in the GIF. We note good linear response in the range of 0.3 to 6.0 Mrads.

As a consequence of film linearity with absorbed energy, beam dose uniformity is readily estimated on the basis of observed, unconverted microdensitometer data.

Evidences of precursor depletion were observed at high integrated doses measured in vacuum environments. At the time of measurement, the loss of response was assumed to be the result of oxygen depletion. Subsequent dosimetry films exposed to identical integrated photon doses both in air and vacuum environments confirmed the oxygen depletion assumption. Other measurements of electron radiation fields, in ambient air environments, further confirmed the oxygen depletion argument in that no loss of detector response, at large integrated doses, was observed.

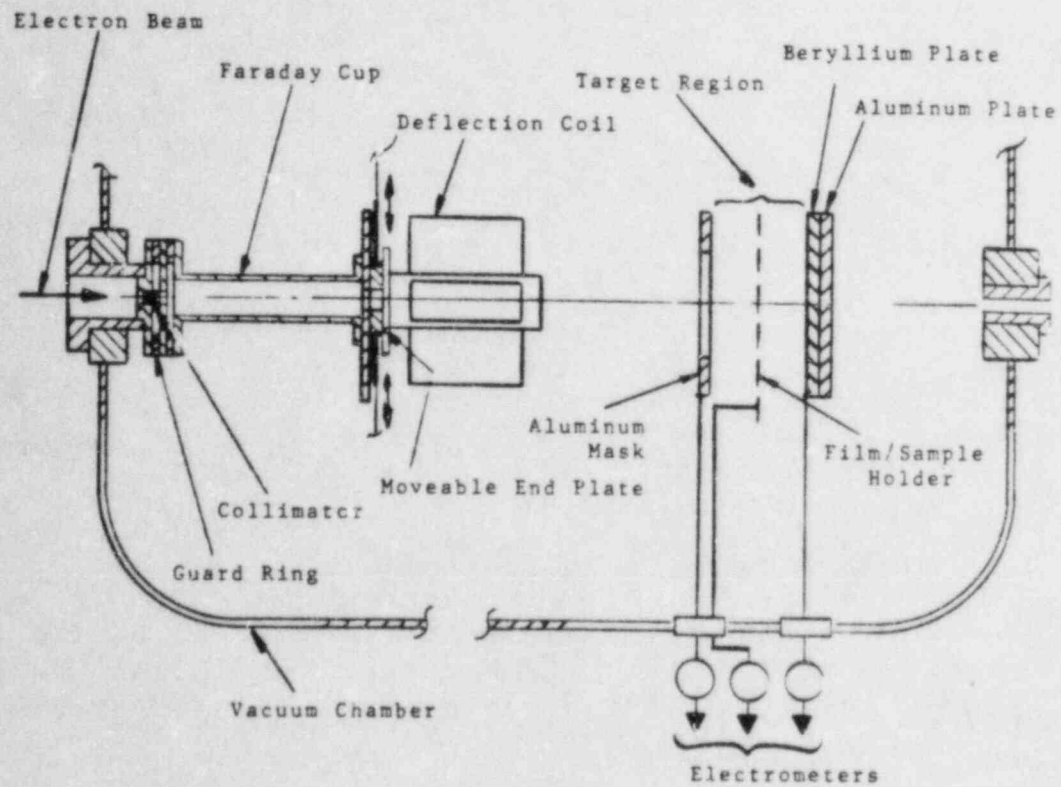


Figure 1: Experiment Configuration in Vacuum Environment

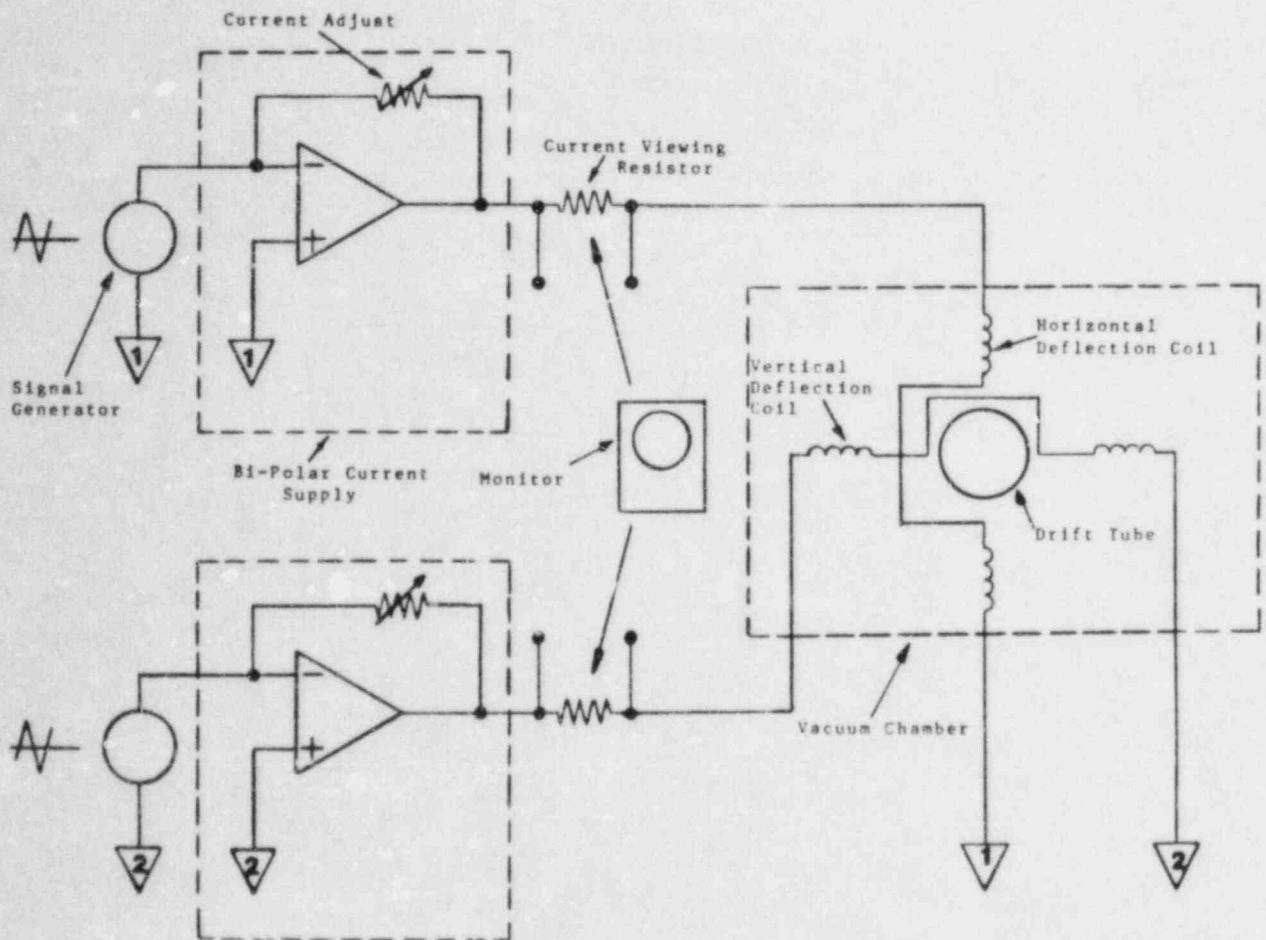


Figure 2: Schematic of the Raster Control System

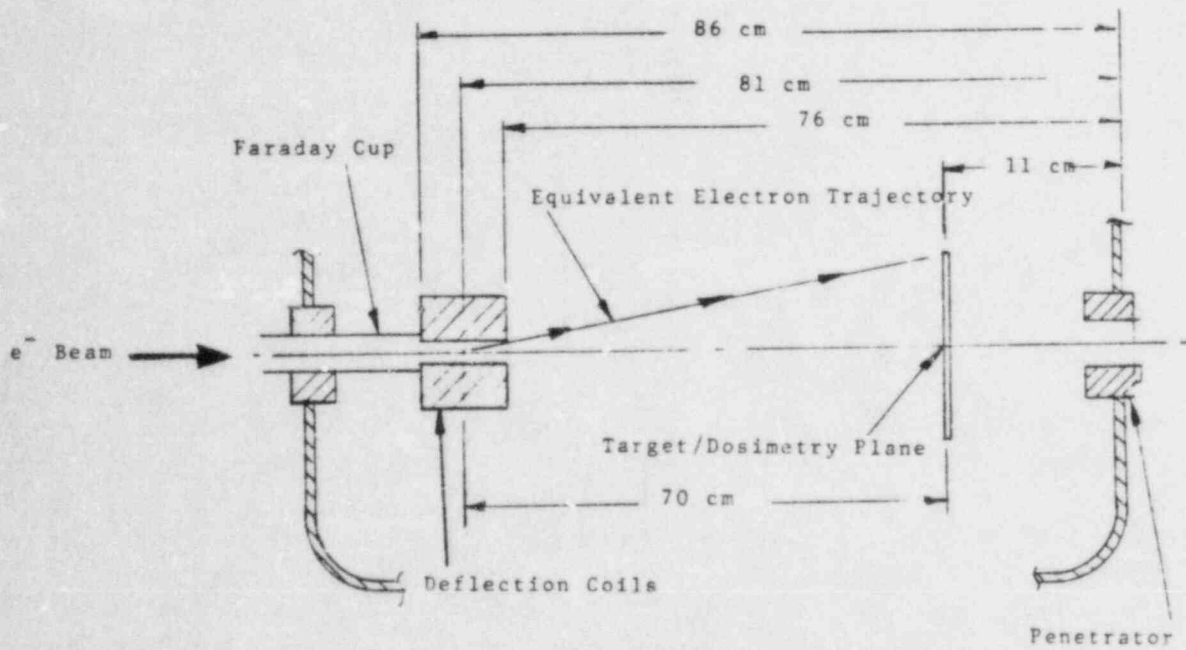


Figure 3: Deflector Coil-Target Geometry in Vacuum Chamber

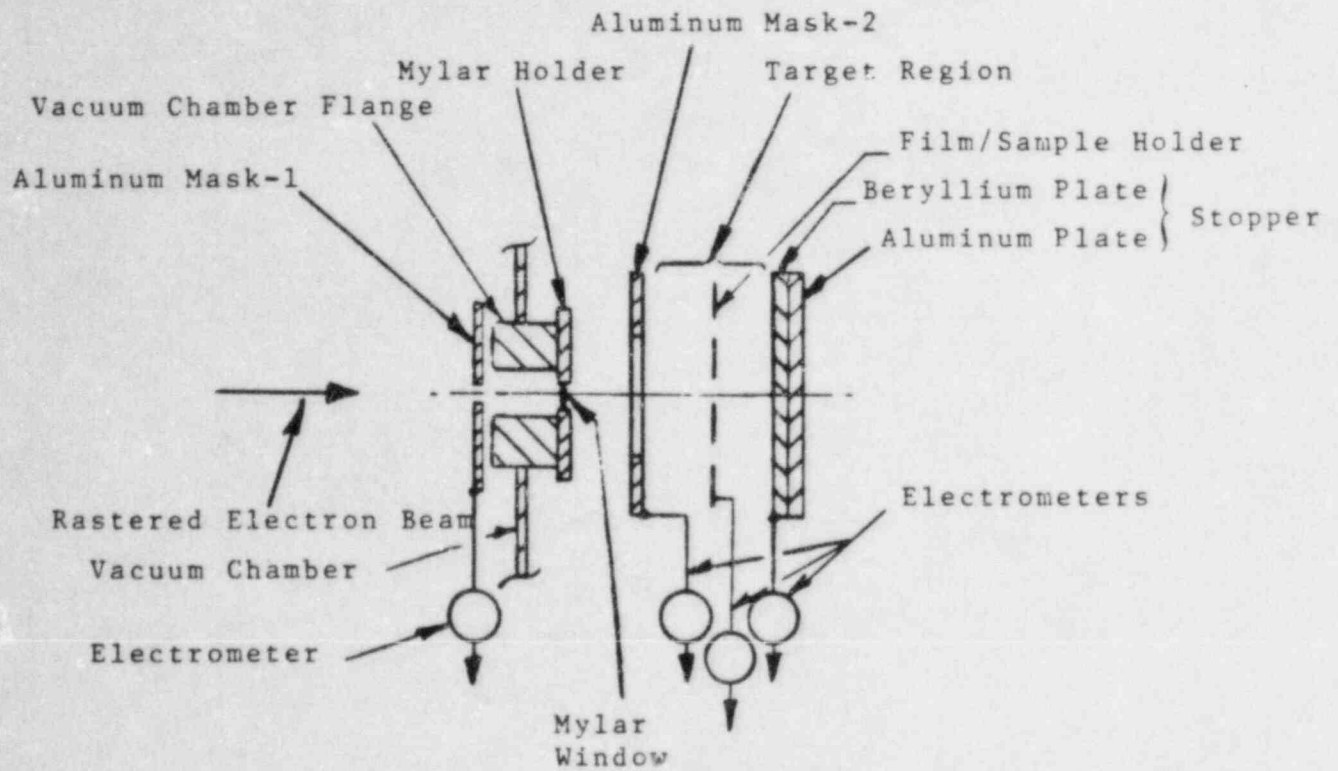


Figure 4: Experiment Configuration in Air Environment

# BEAM PATTERN for EQUAL DEFLECTION CURRENTS

Horizontal Scan  
F = 100 Hz

Vertical Scan  
F = 33 Hz

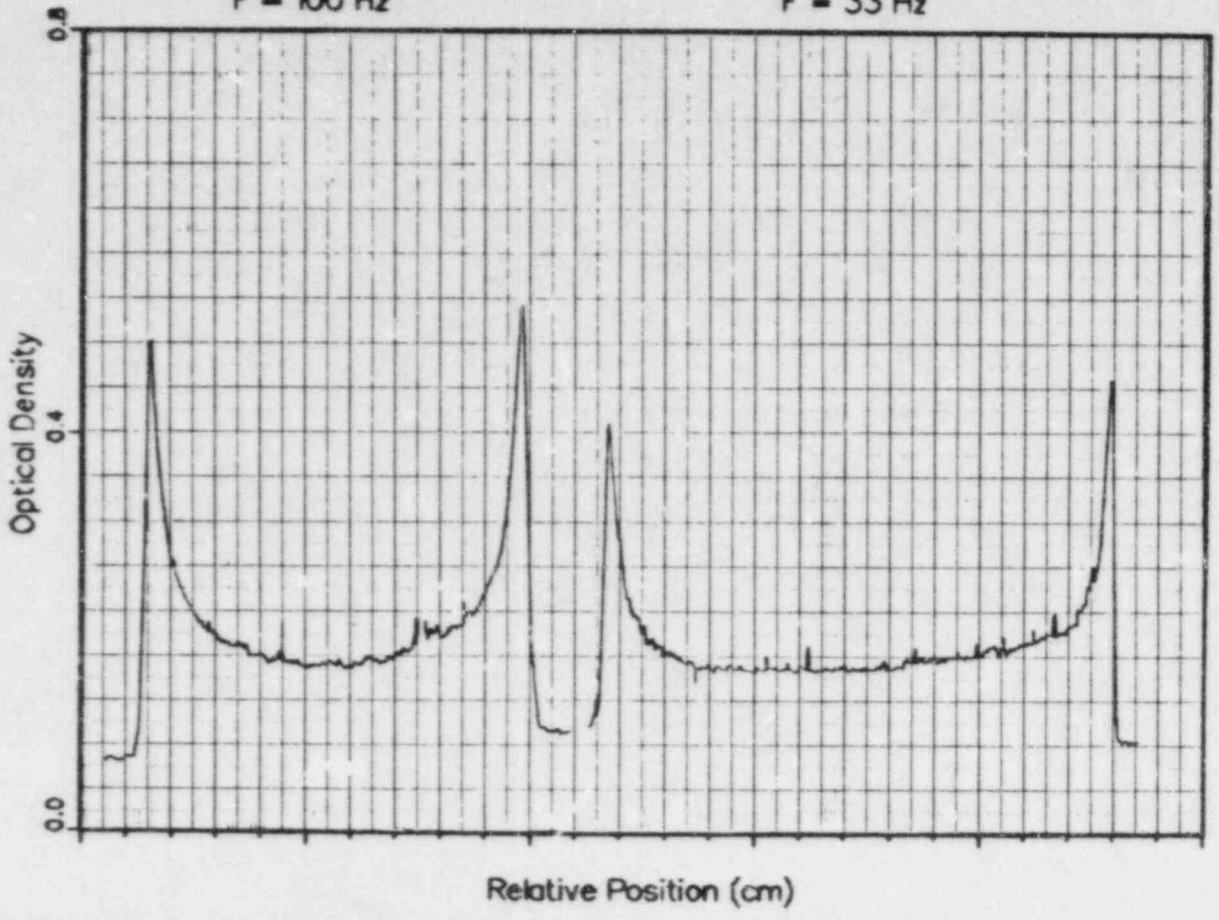


Figure 5: Electron Beam Pattern for Equal Deflection Coil Current



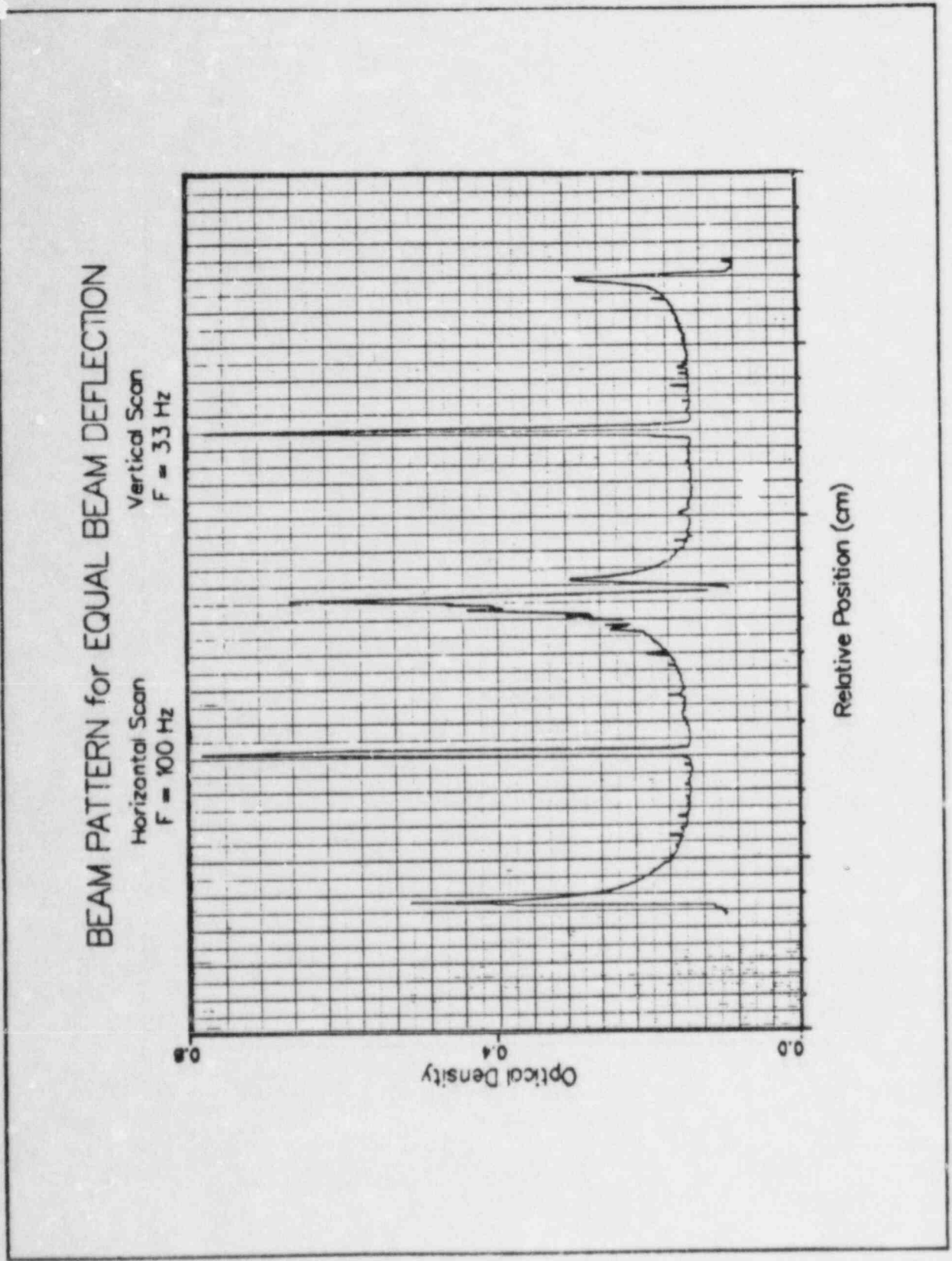


Figure 6: Electron Beam Pattern for Equal Beam Deflection

BEAM PATTERN BEHIND MASK

Horizontal Scan  
F = 100 Hz

Vertical Scan  
F = 33 Hz

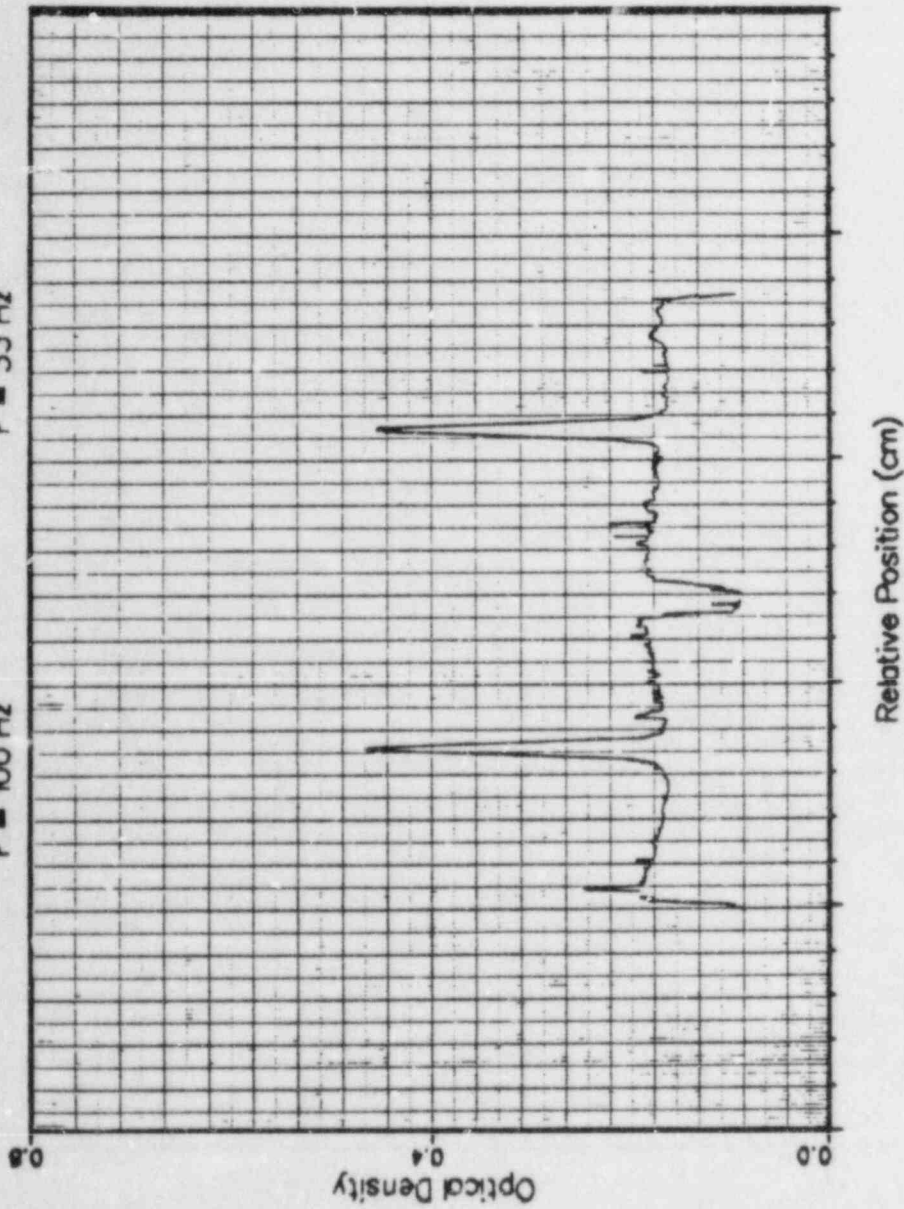


Figure 7: Electron Beam Pattern Behind Mask

# BEAM CURRENT PARTITION

Beam Energy = 1.0 MeV

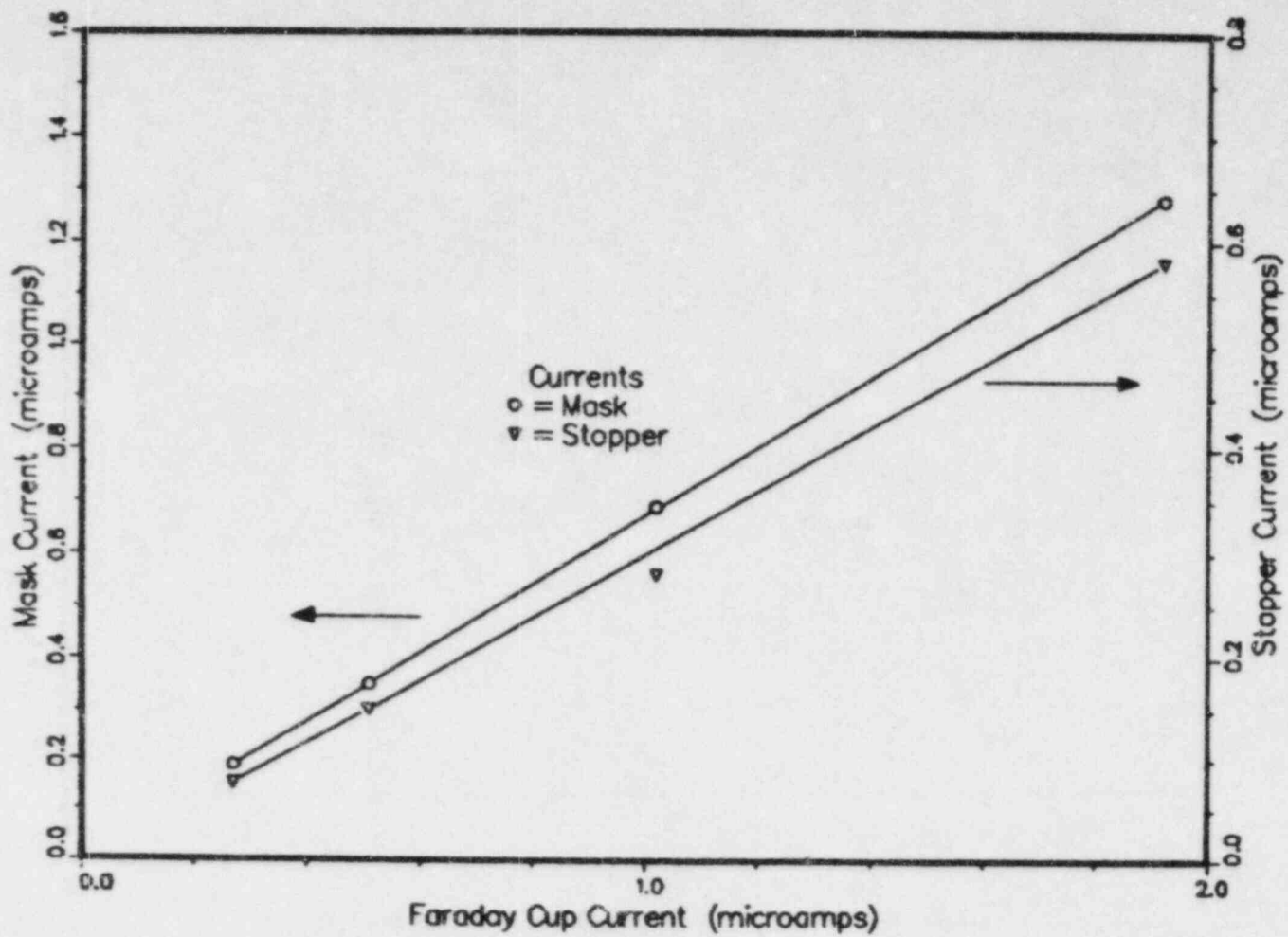


Figure 8: Beam Current Partition

# DOSIMETER RESPONSE versus ELECTRON ENERGY

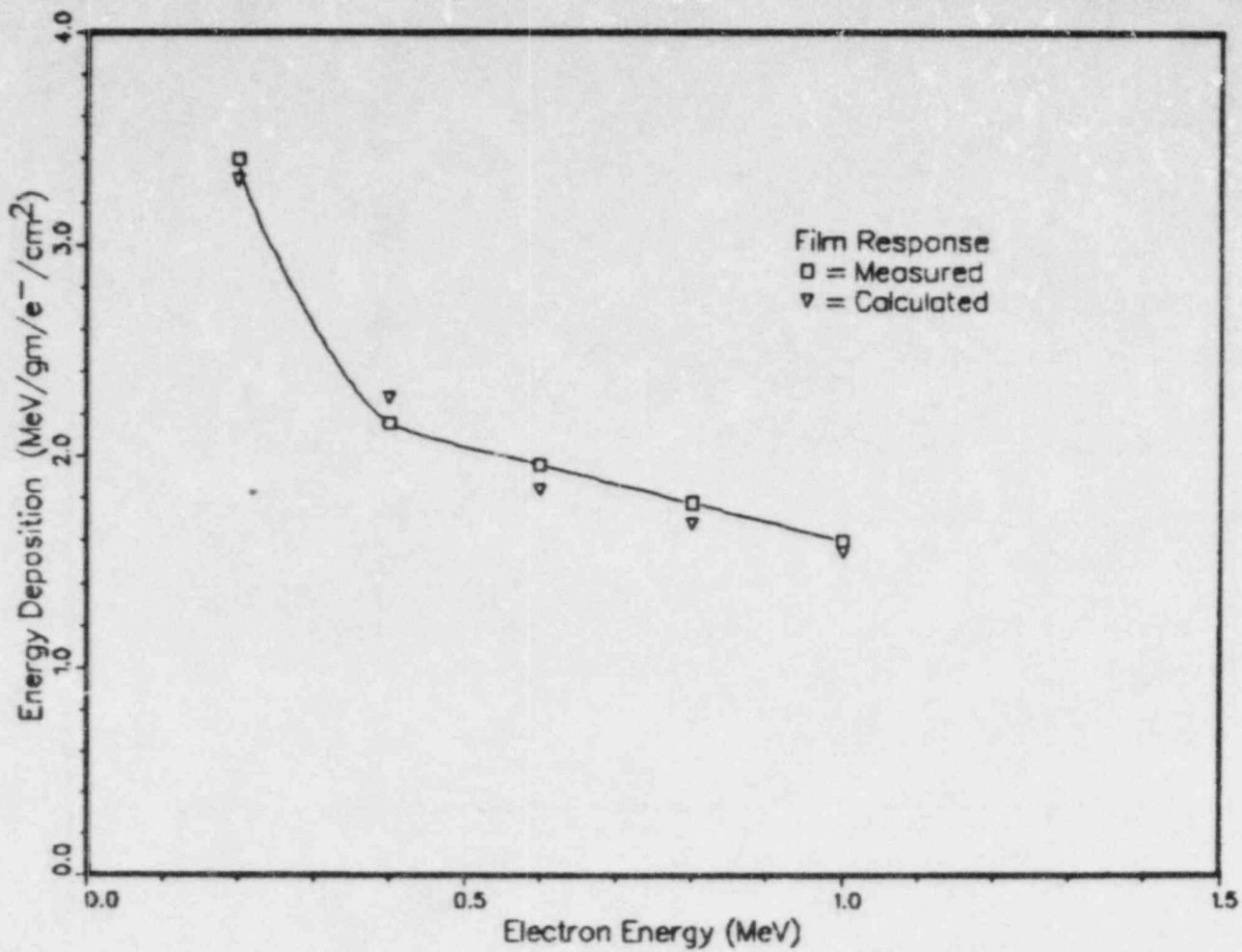


Figure 9: Dosimeter Response Versus Electron Energy

# DOSE versus STOPPER CURRENT

Measured and Calculated Results

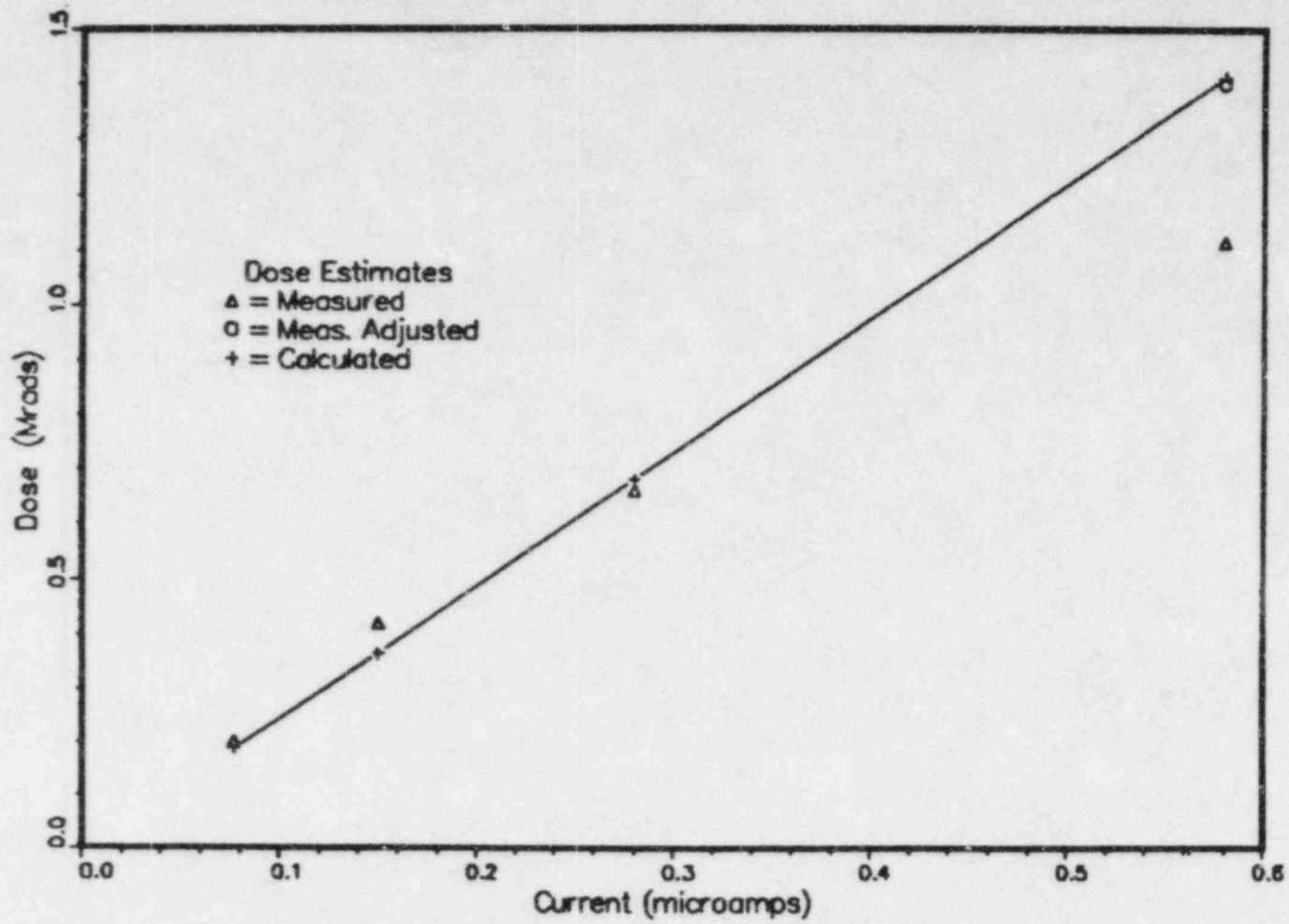
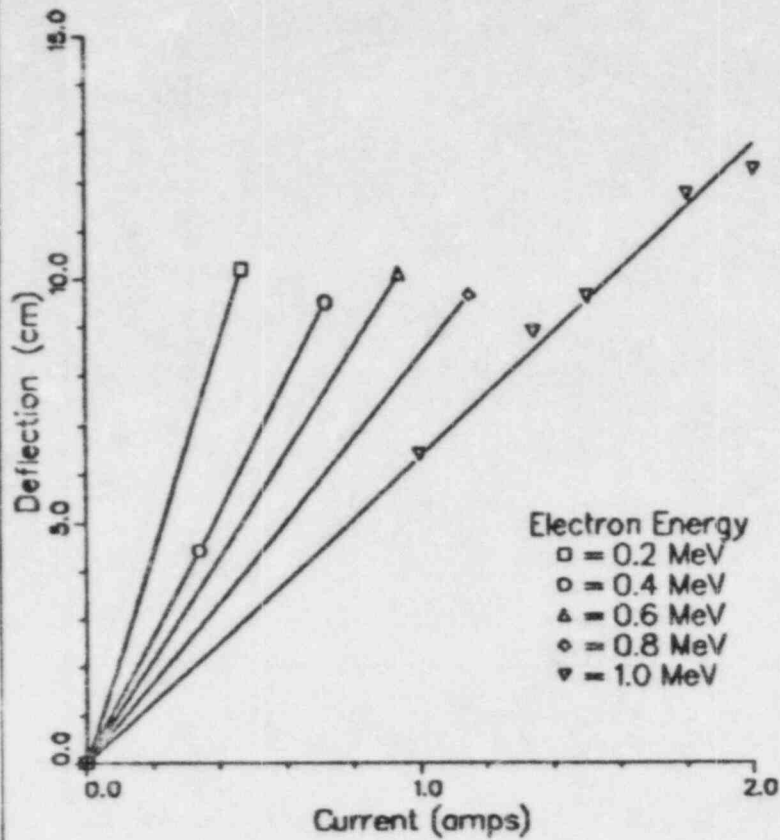


Figure 10: Dose Versus Stopper Current for 1.0 MeV Electrons

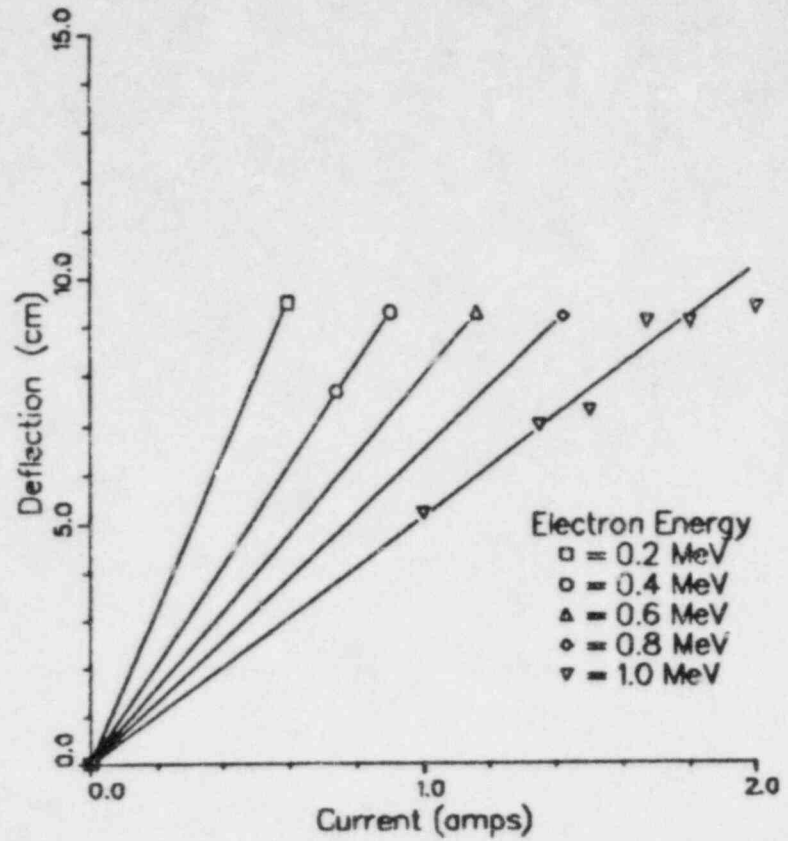
Figure 11: Beam Deflection as a Function of Coil Current

### BEAM DEFLECTION versus COIL CURRENT

Frequency = 33 Hz



Frequency = 100 Hz



# BEAM DEFLECTION versus CURRENT FREQUENCY

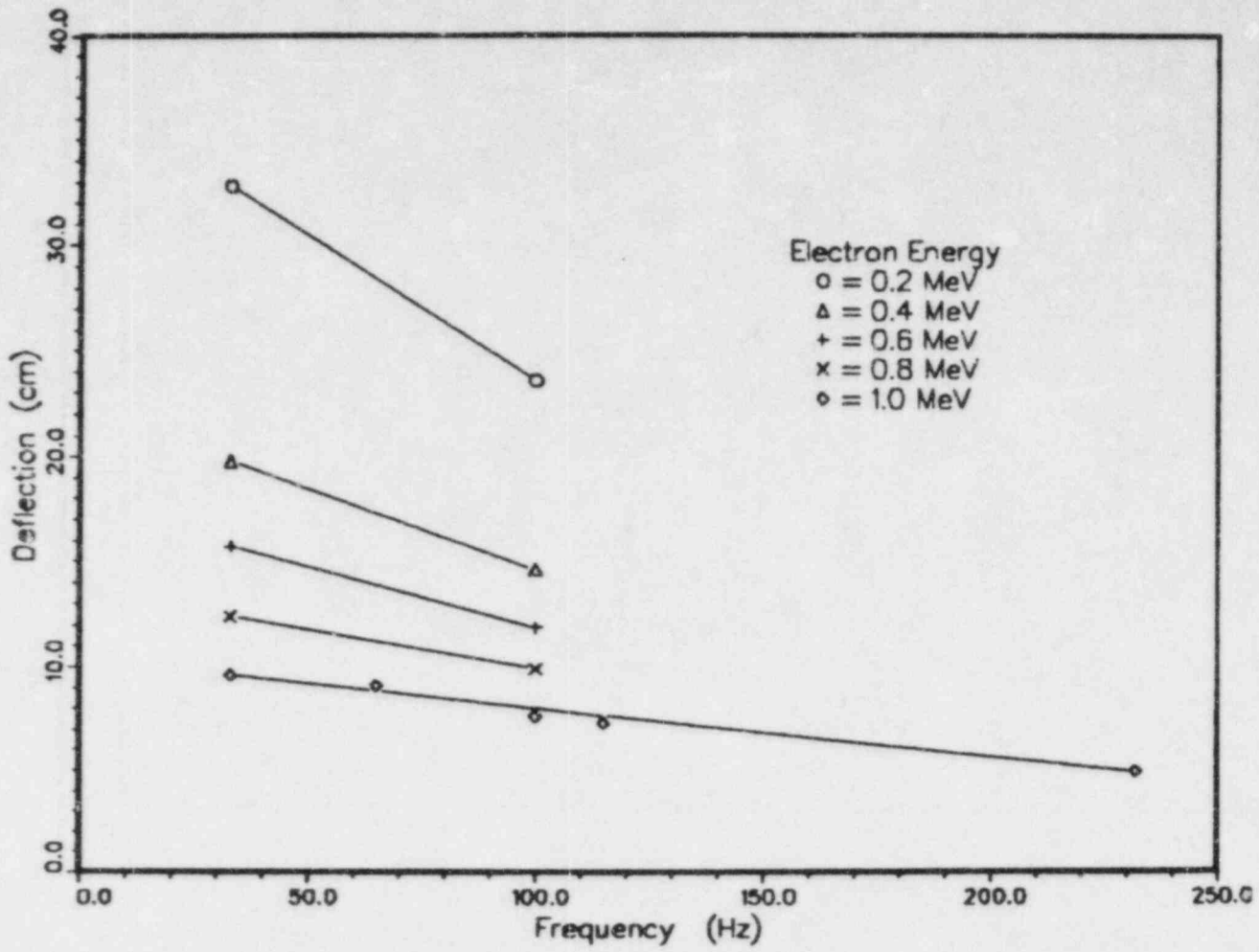


Figure 12: Beam Deflection as a Function of Coil Current Frequency

# BEAM DEFLECTION versus ELECTRON ENERGY

Coil Current = 1.0 Ampere

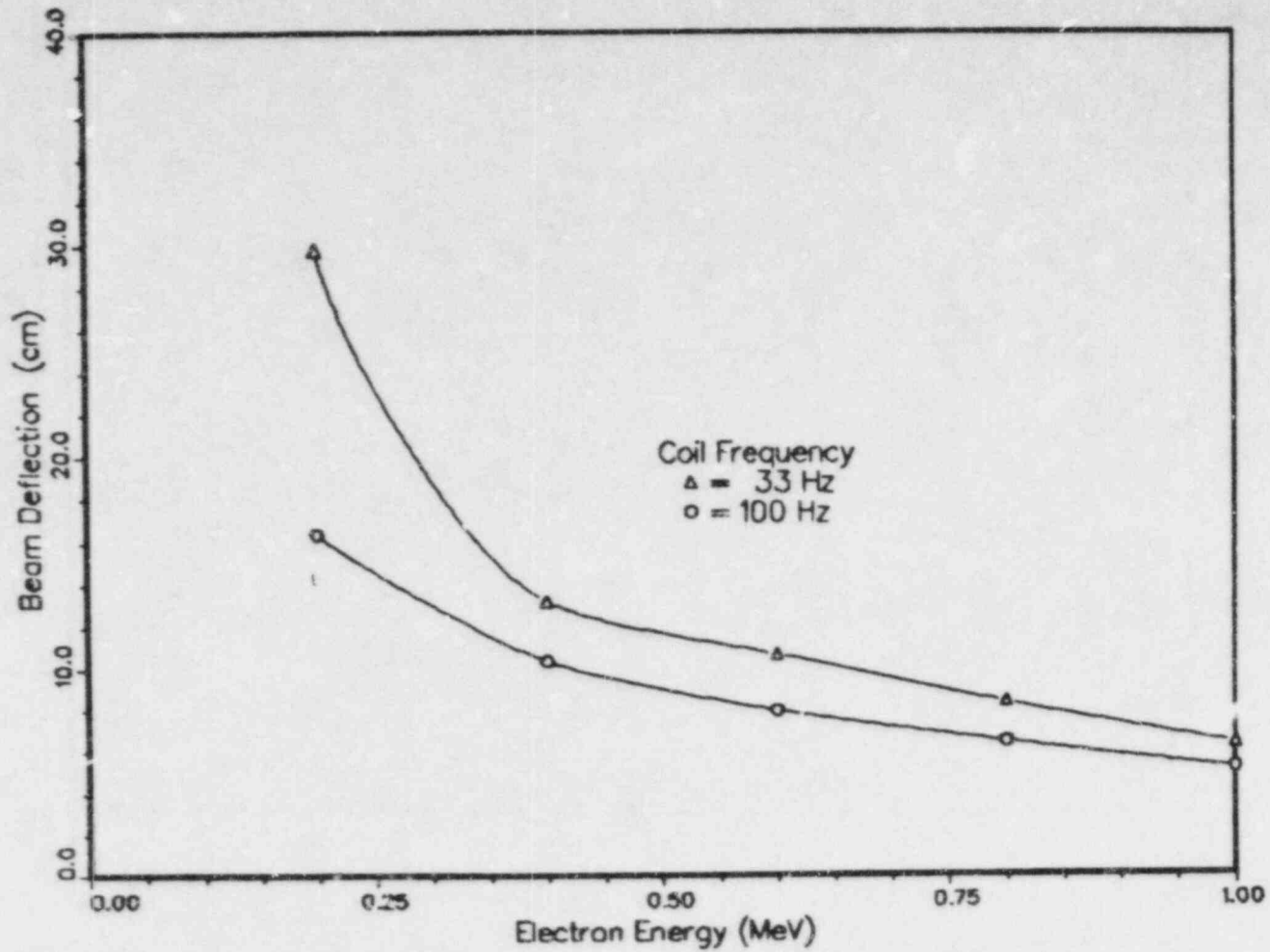
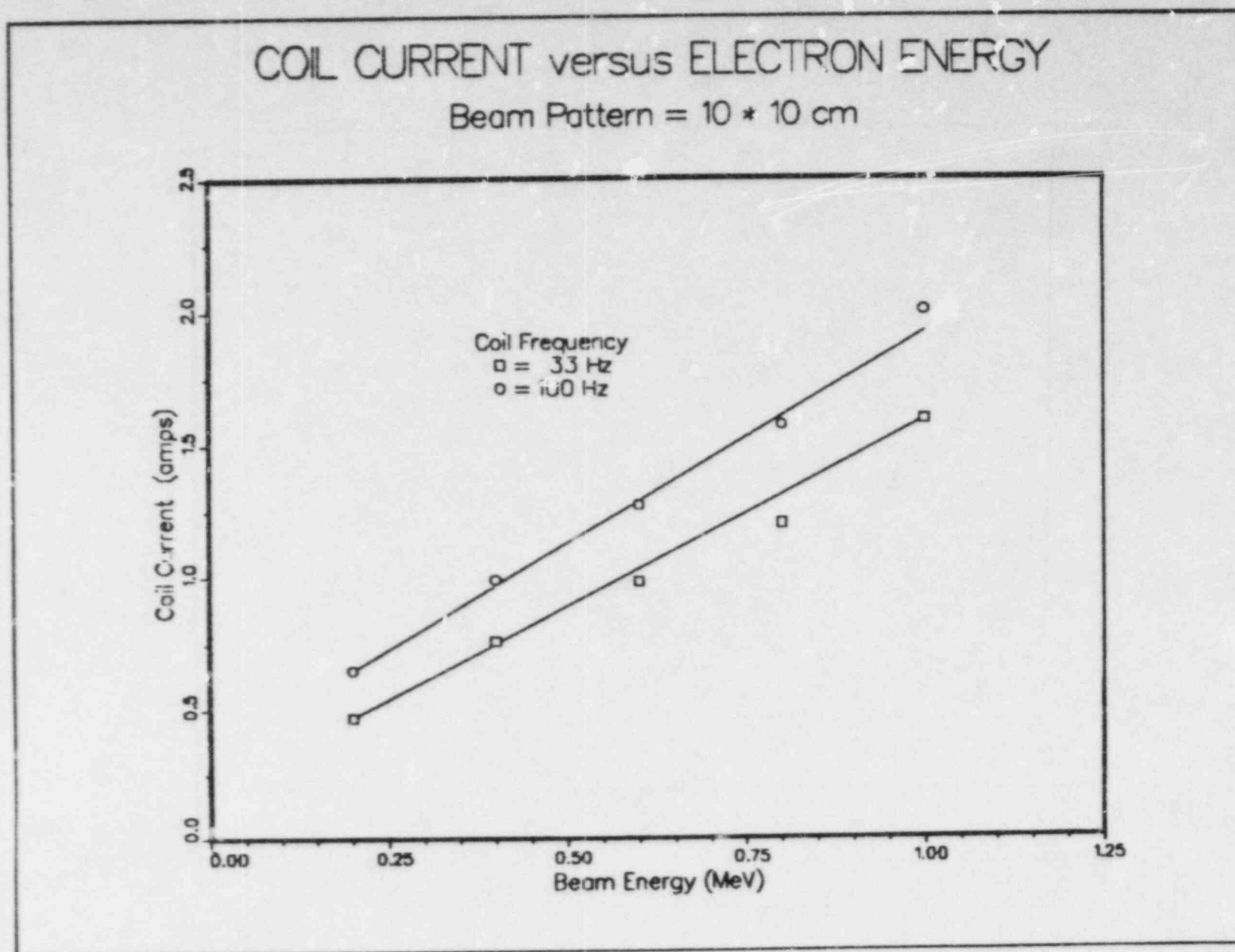


Figure 13: Beam Deflection as a Function of Electron Energy



Figure 14: Coil Current Versus Electron Energy



# DOSE versus STOPPER CURRENT

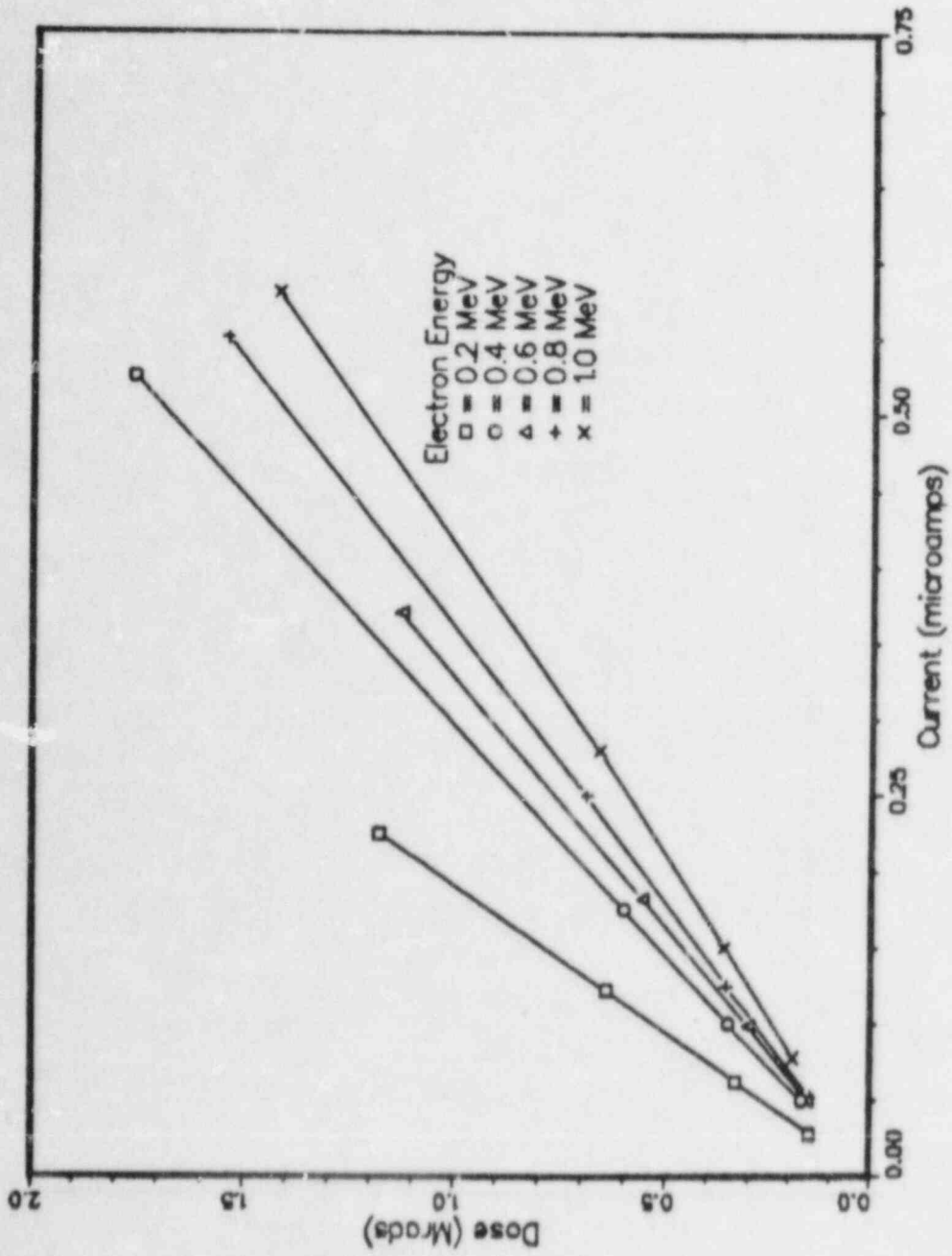
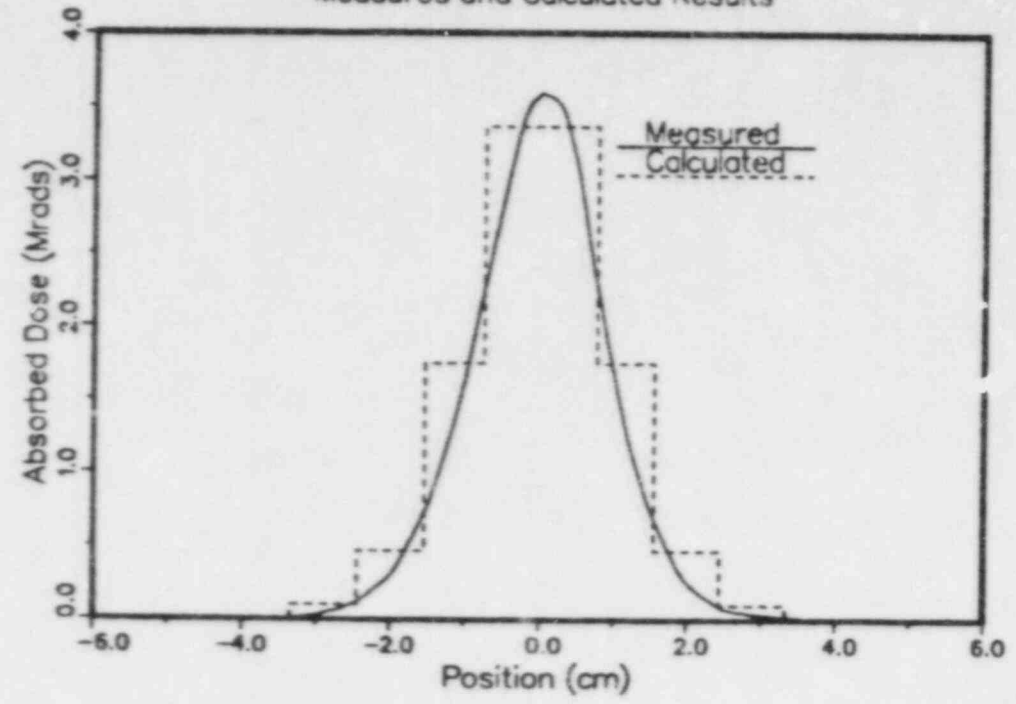


Figure 15: Dose as a Function of Stopper Current

Figure 16: Electron Beam Dose Versus Position Following 1.0 MeV Electron Transport Through 0.025-cm Beryllium

Electron Beam Dose vs Position  
in Target Plane following 1.0 MeV  
Beam Transport Through 0.025-cm Be  
Measured and Calculated Results



Calculated Dose versus Position in Target Plane  
for  
Electron Transport Through 0.00254 Mylar

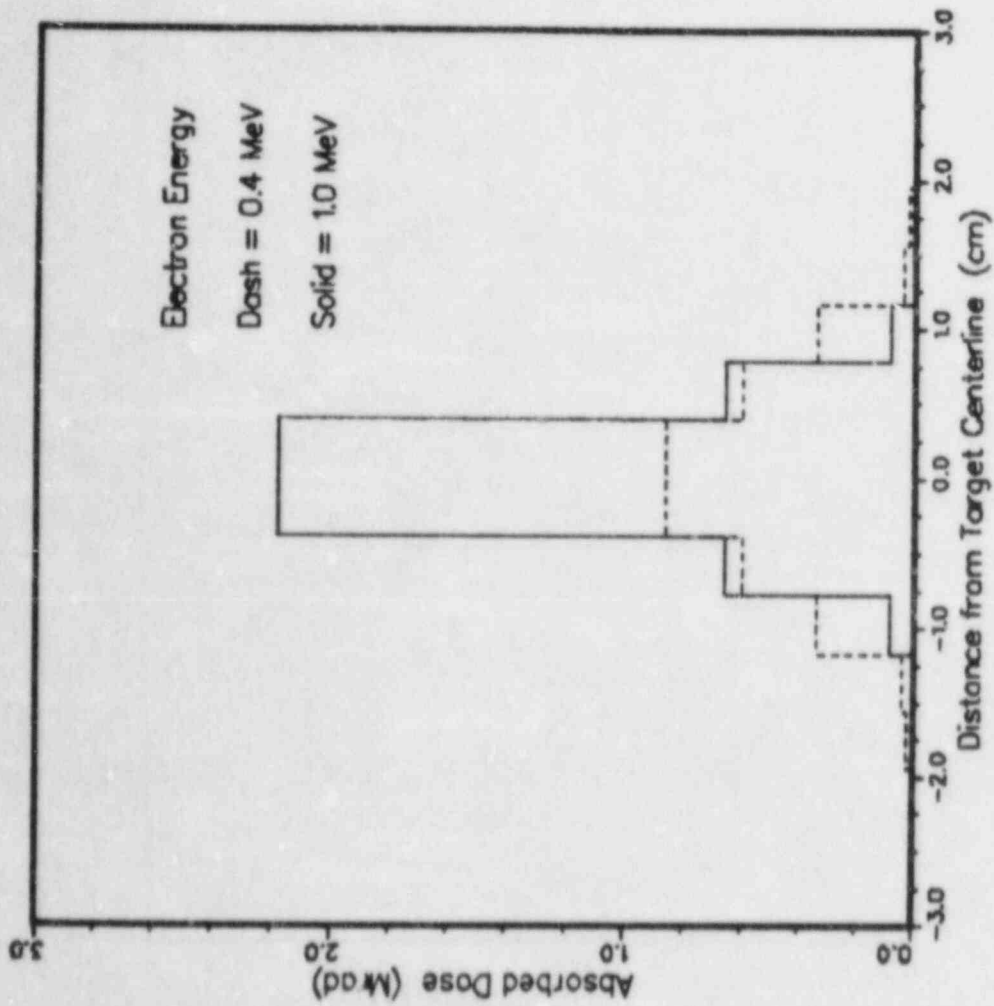


Figure 17: Dose Versus Position

# 1.0 MeV RASTERED BEAM TRANSPORT

.00254 cm MYLAR TARGET

Film Traverse : Horizontal      Vertical

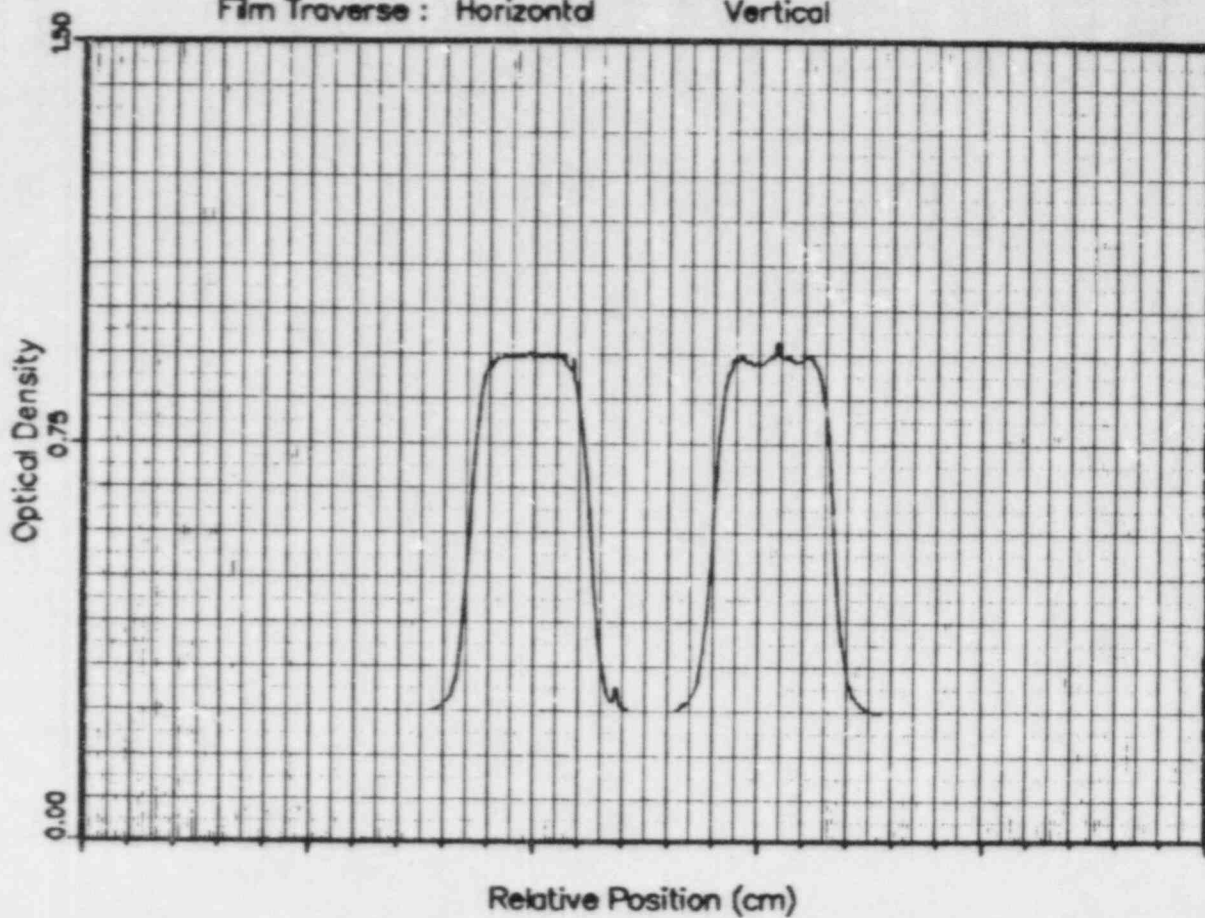
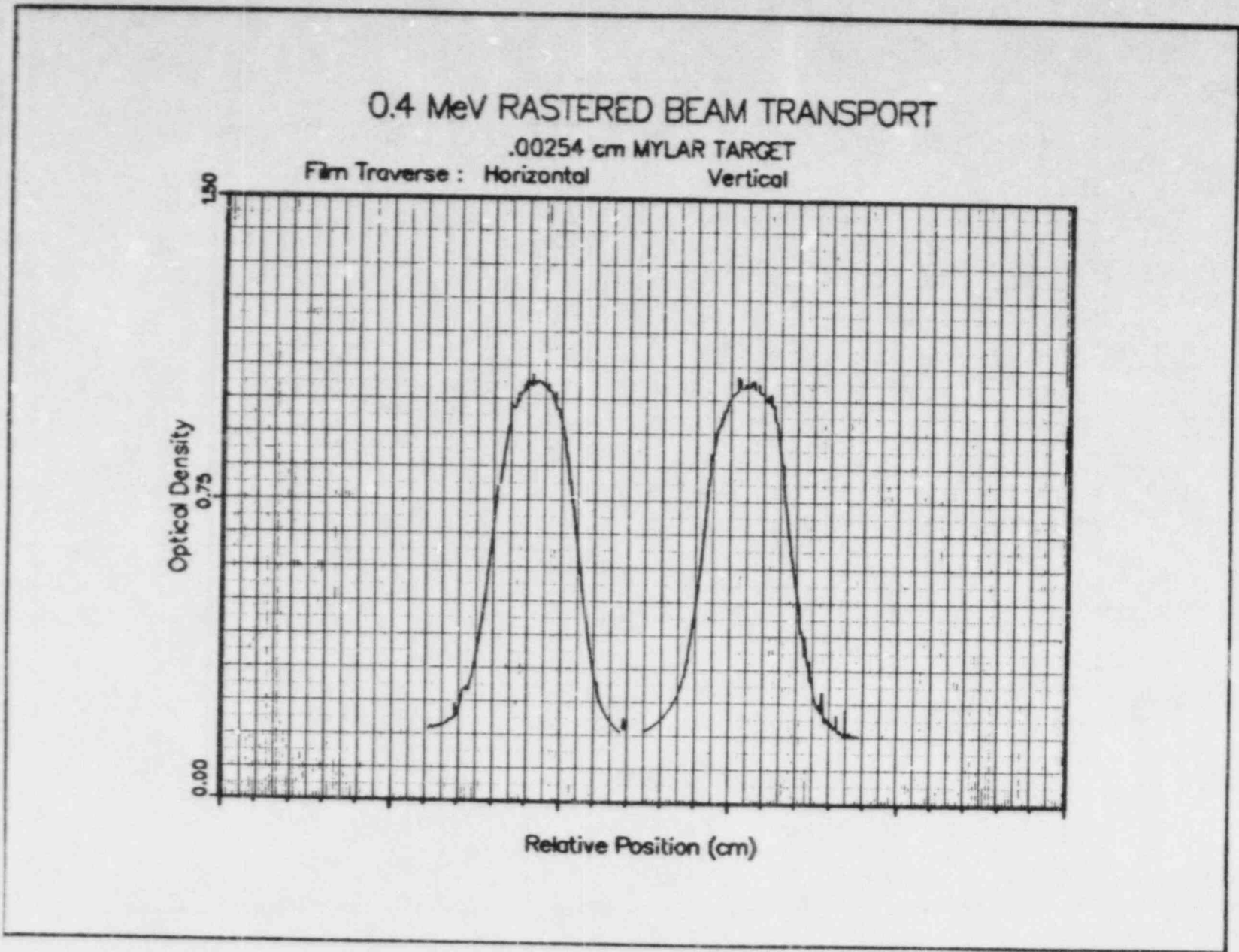


Figure 18: Electron Beam Pattern for 1.0 MeV Rastered Beam Transport Through 0.0025-cm Mylar Film

Figure 19: Electron Beam Pattern for 0.4 MeV Rastered Beam Transport Through 0.0025-cm Mylar Film



1.0 MeV RASTERED BEAM  
TRANSPORT IN AIR  
Film Location : Target Zone Behind Mask 2

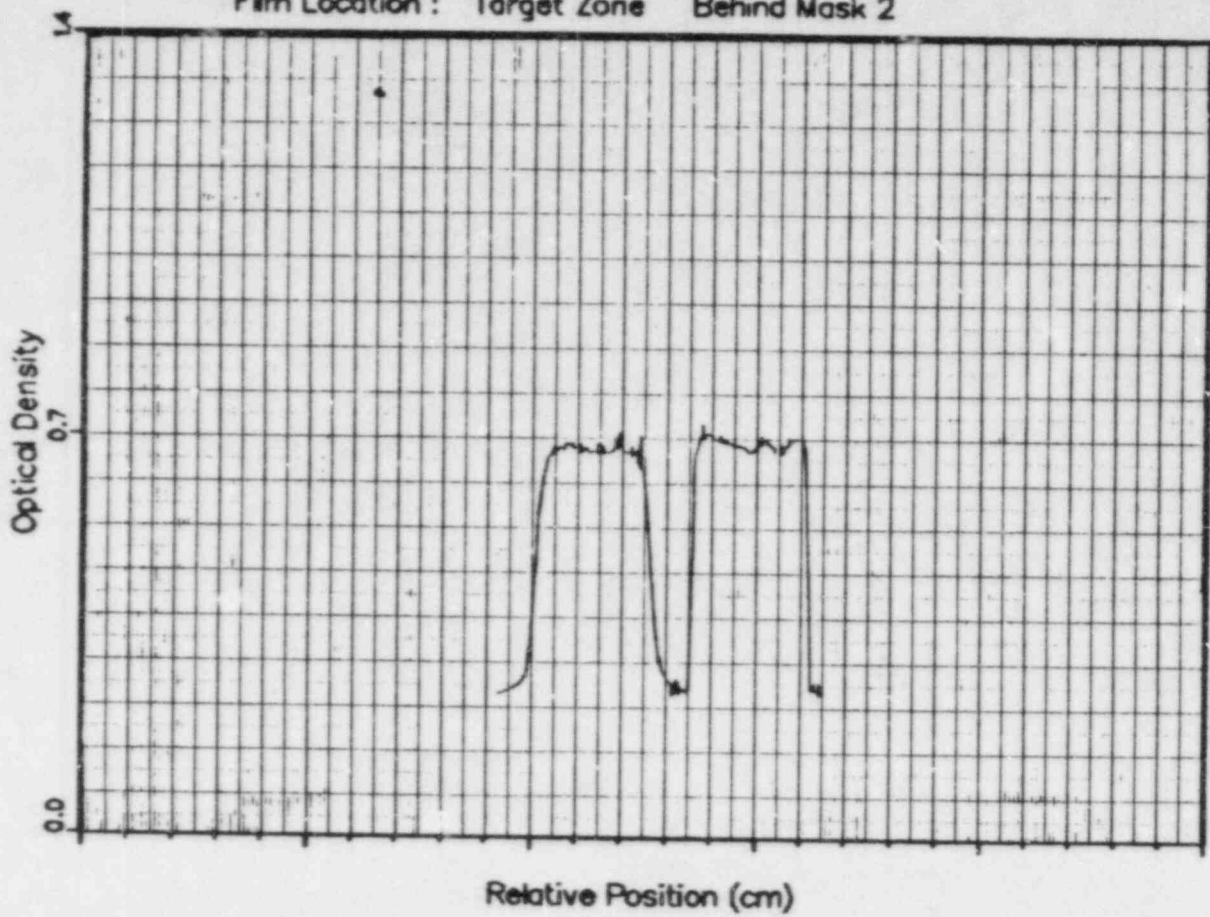


Figure 20: Electron Beam Pattern for 1.0 MeV Rastered Beam  
Transport in Air

# 0.4 MeV RASTERED BEAM

TRANSPORT IN AIR

Film Location: Target Zone Behind Mask 2

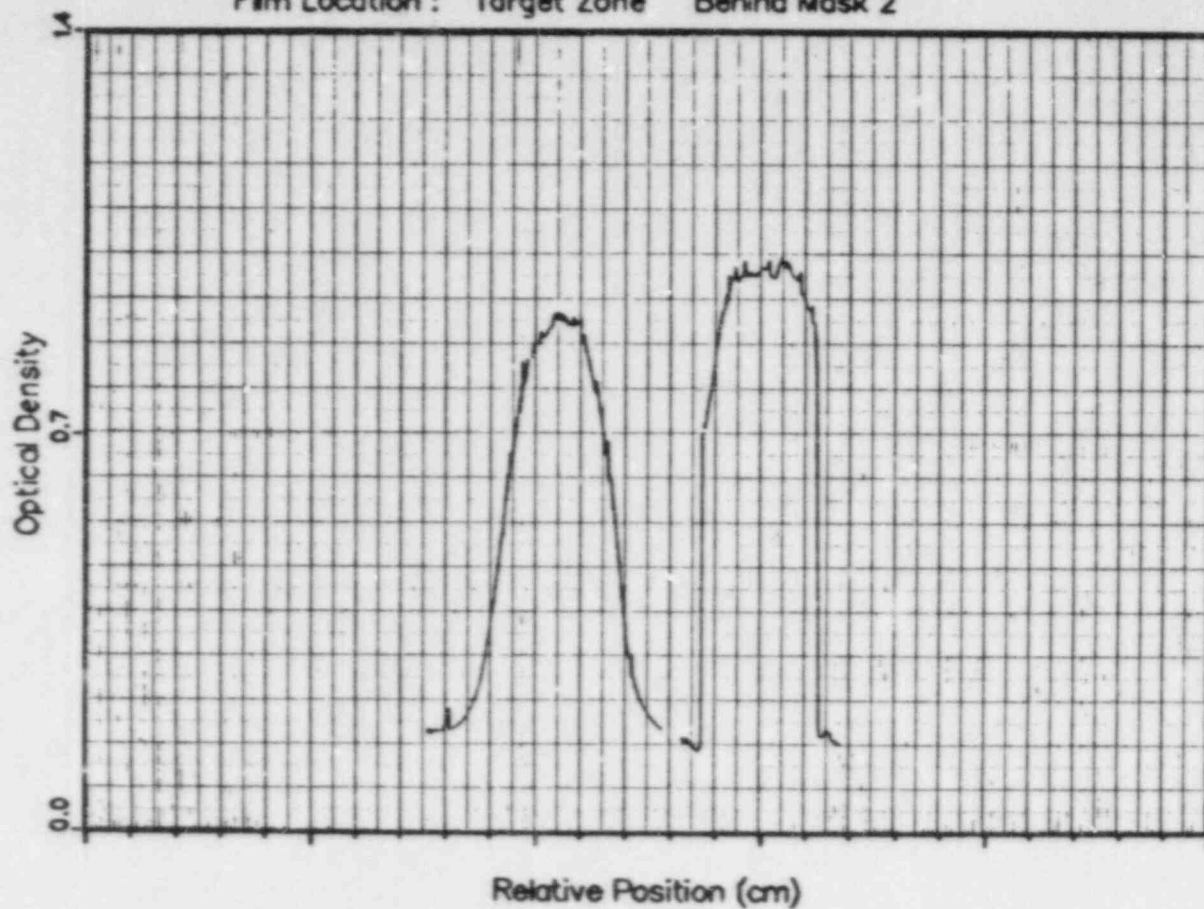
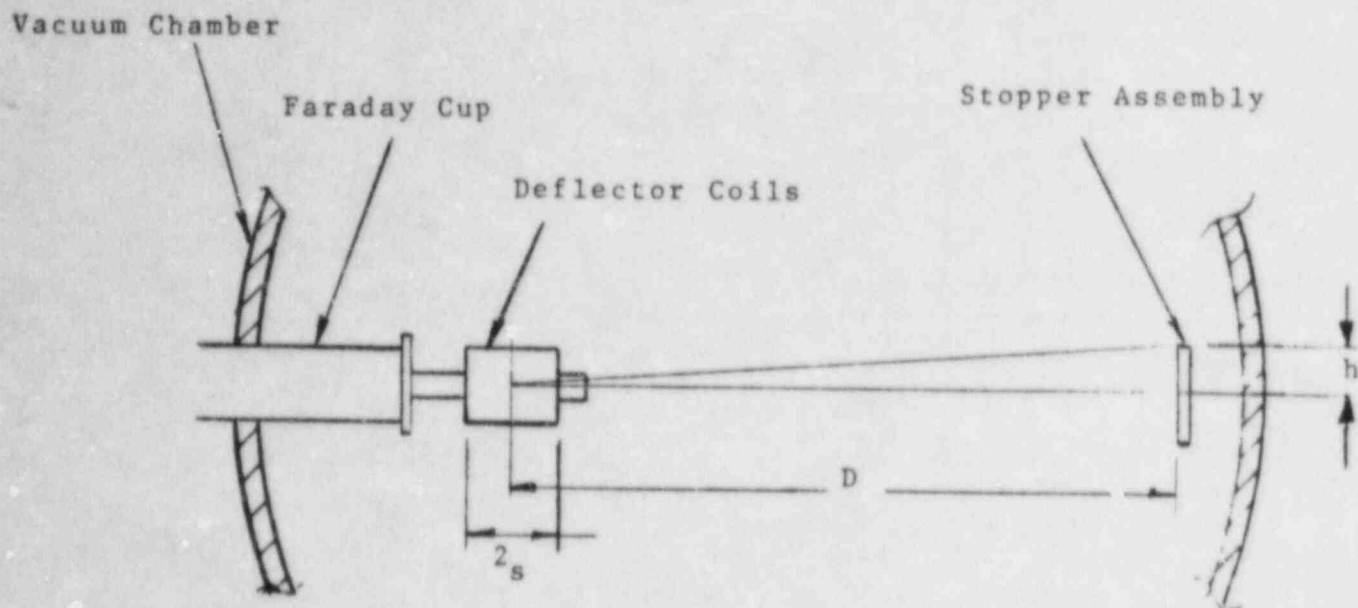
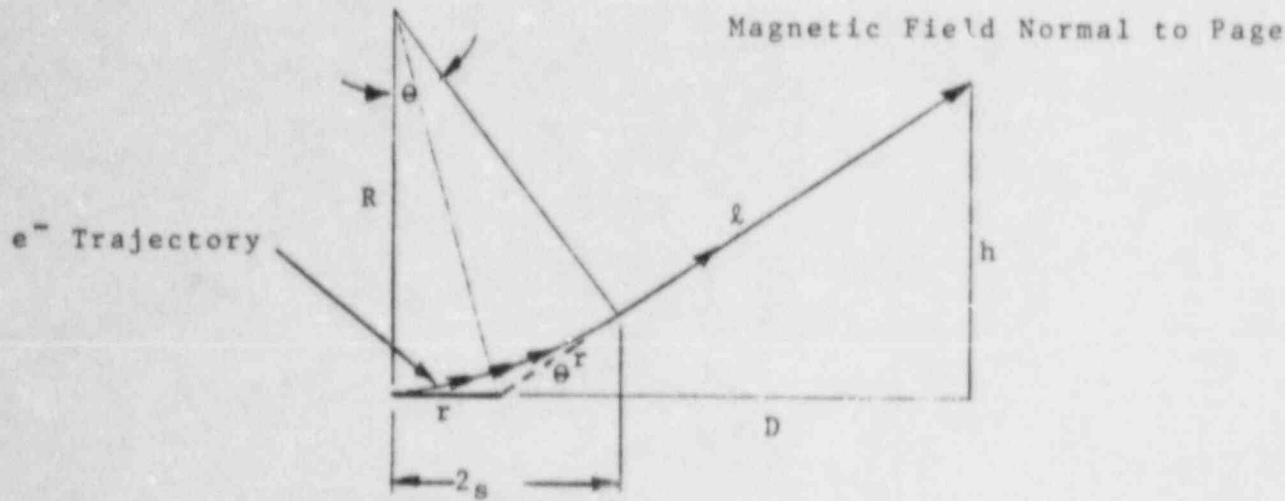


Figure 21: Electron Beam Pattern for 0.4 MeV Rastered Beam Transport in Air





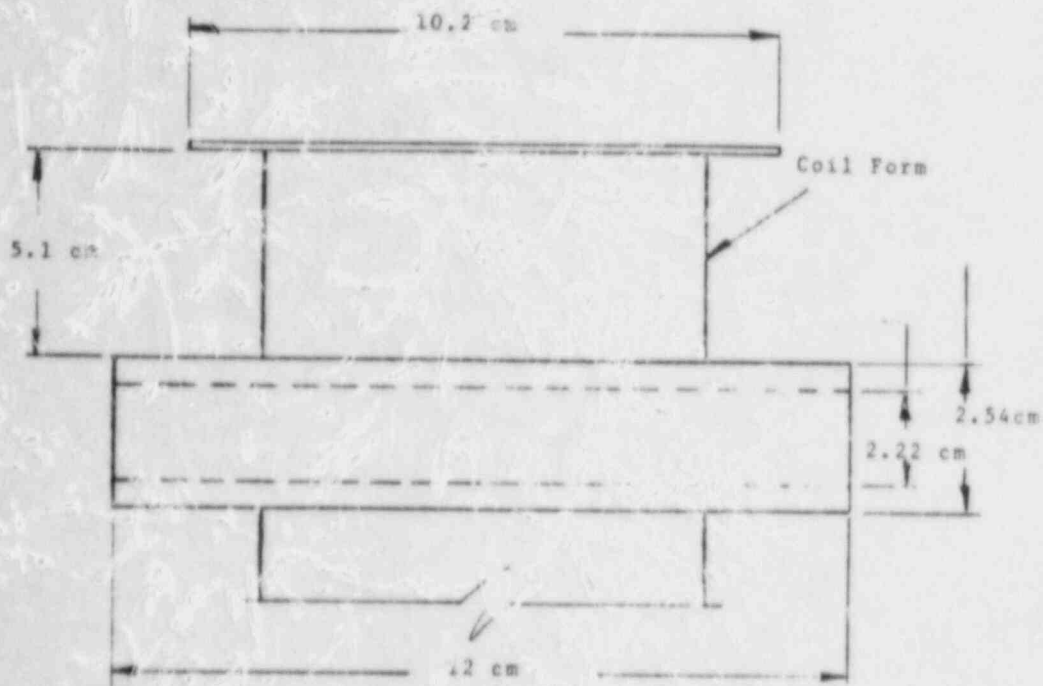
(a)



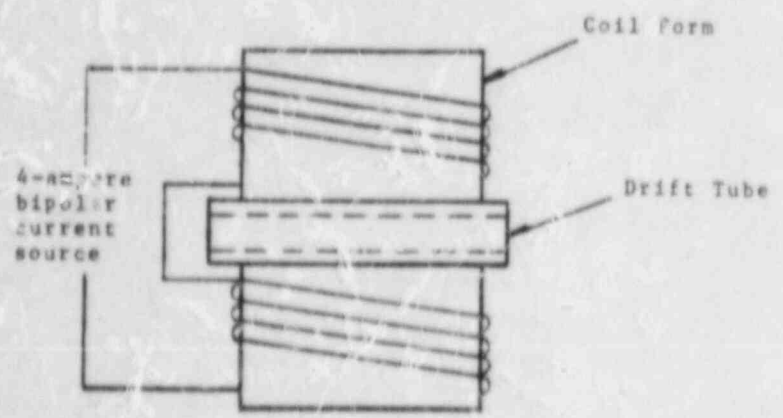
(b)

Figure 22: (a) Schematic of Deflector Coil-Target Geometry

(b) Electron Beam Trajectory in Uniform Magnetic Field



(a)



(b)

Figure 20. (a) Deflector Coil Dimensions

(b) Deflector Coil Wiring Configuration

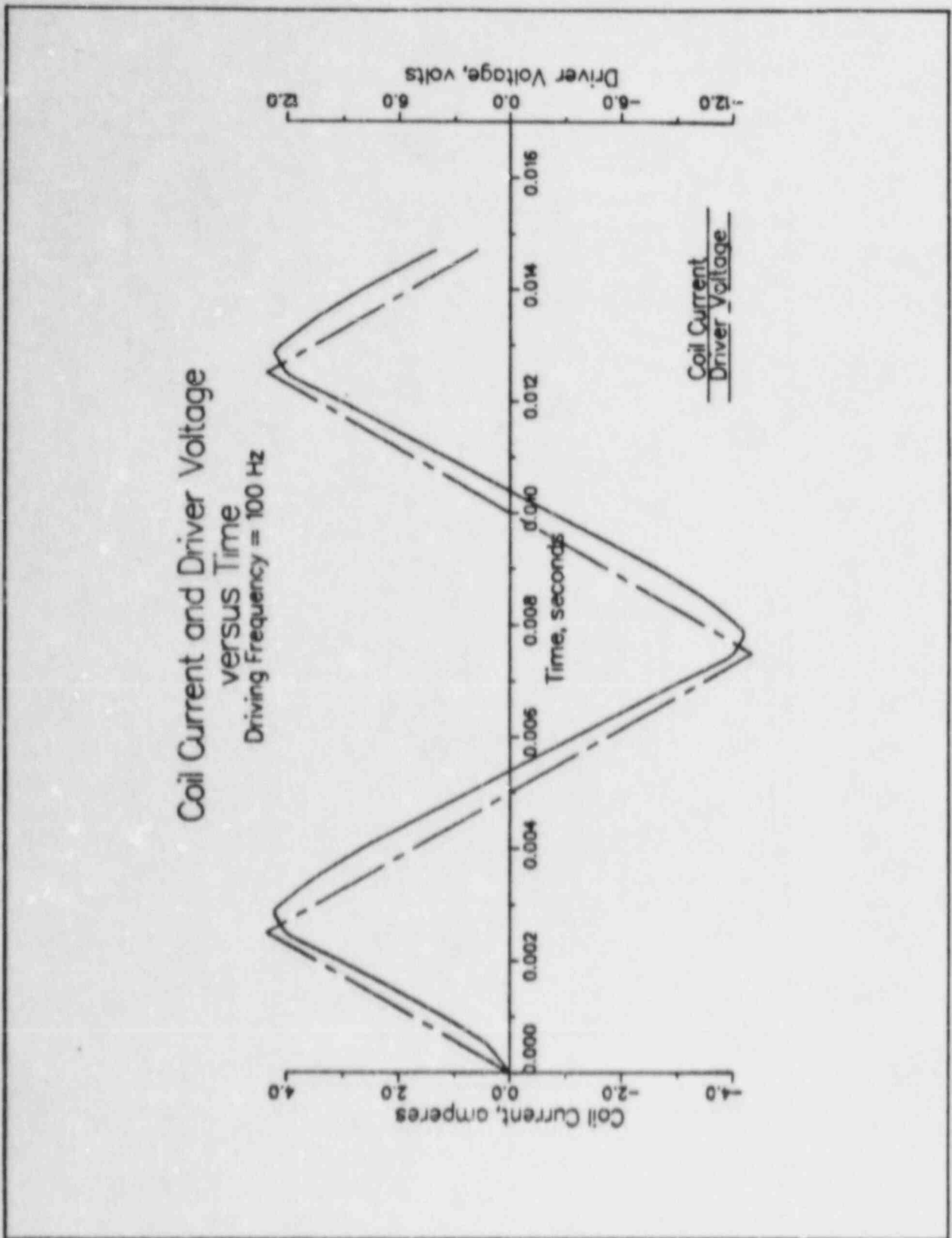


Figure 24: Coil Current and Driver Voltage as a Function of Time

# MAGNETIC FIELD INTENSITY versus ELECTRON ENERGY

Electron Deflection = 3.8 cm

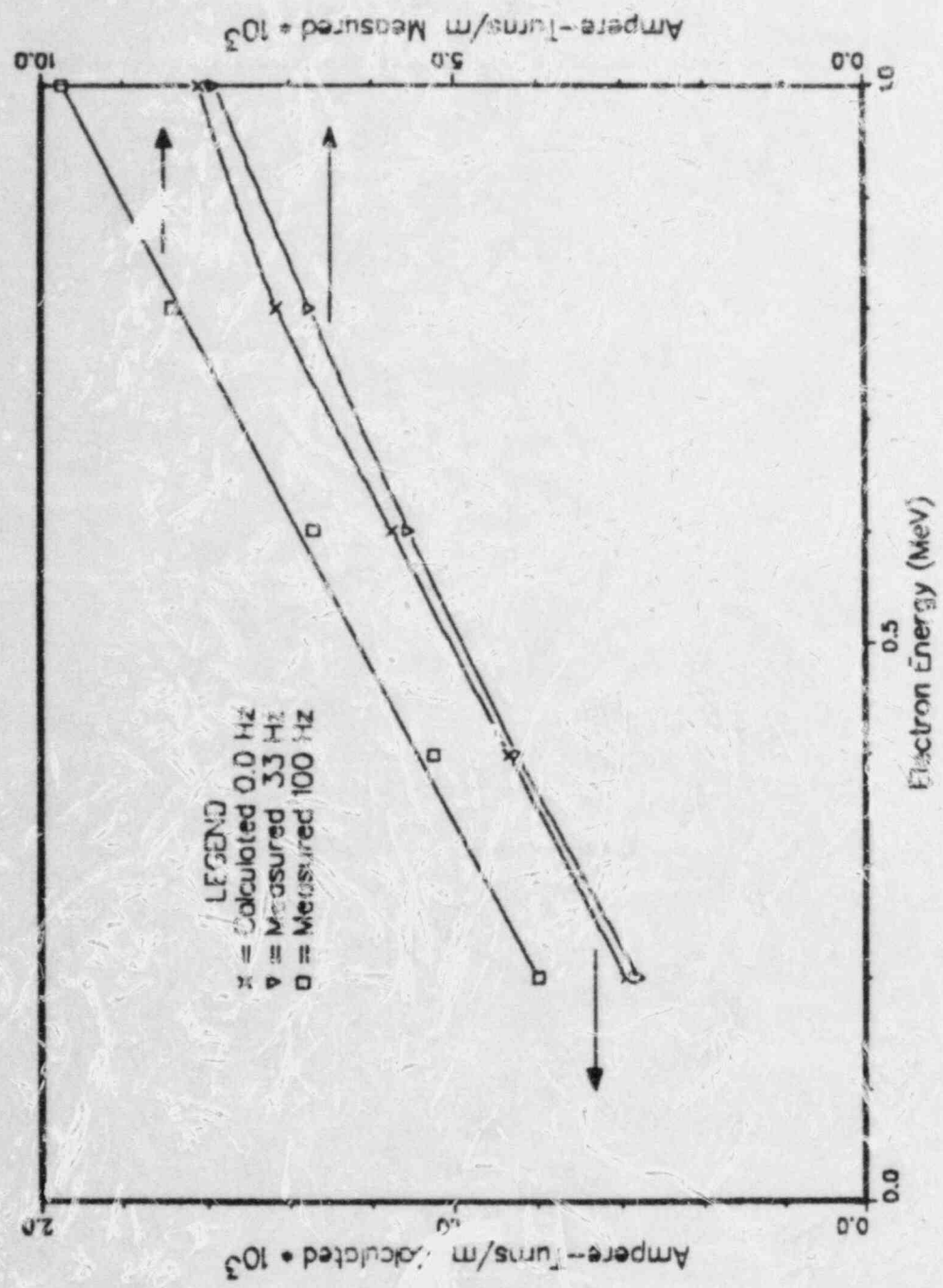


Figure 25: Magnetic Field Intensity Versus Electron Energy Measured and Calculated Results

# OPTICAL DENSITY versus ABSORBED DOSE

Chlorostyrene and Nylon Calibration Data

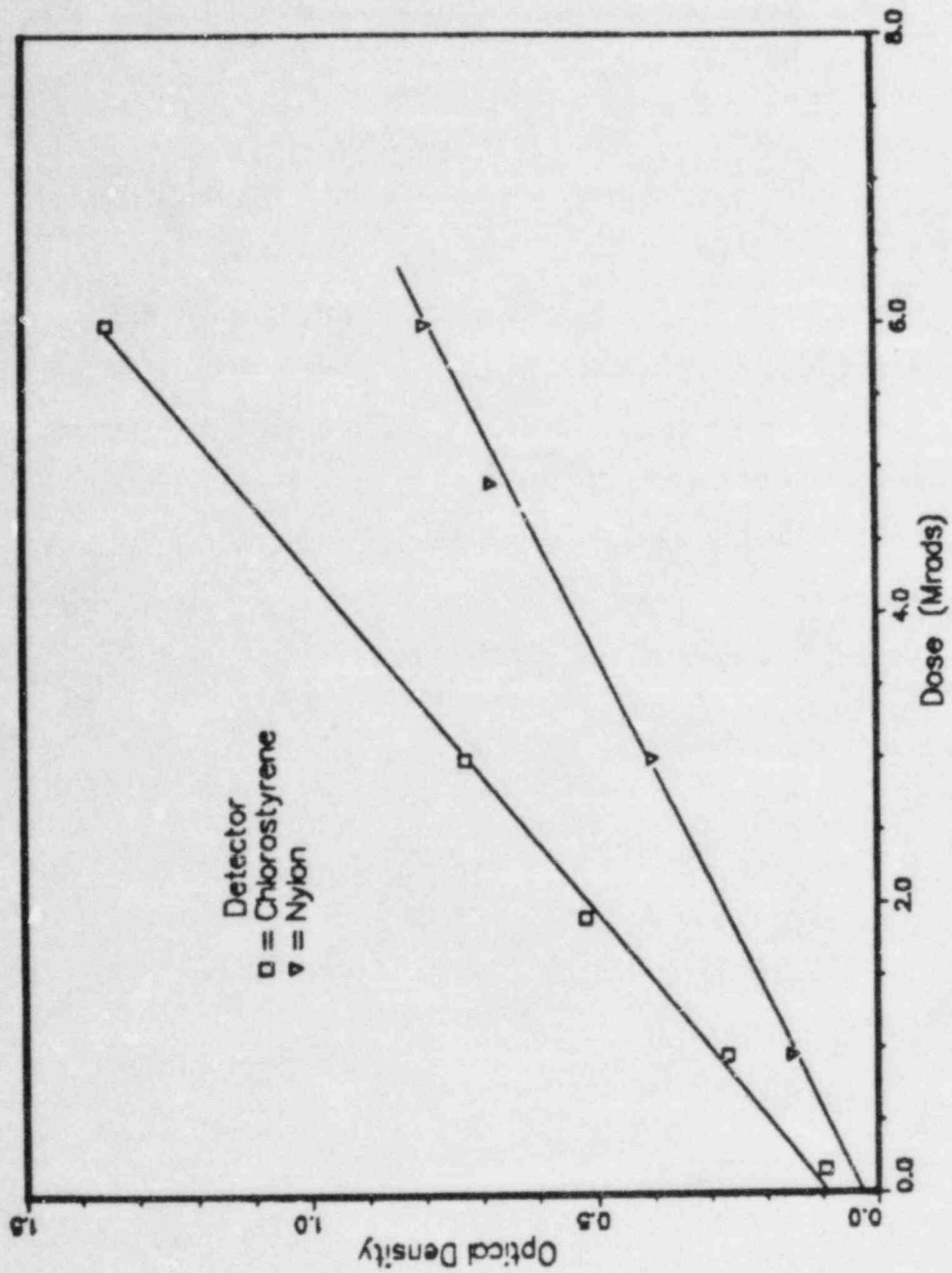


Figure 26: Dosimeter Response - Optical Density Versus Absorbed Dose

TABLE I  
 PELLETRON and RASTER SYSTEM SPECIFICATIONS

Accelerator Type	-----	:	Monoenergetic , Steady State
Energy Range	-----	:	0.025 - 1.2 MeV Continuously Variable
Beam Energy Uncertainty	-----	:	~0.5 %
Beam Current Range	-----	:	0.001 - 34 microamperes
Raster-Target Separation (Vacuum)	--	:	0.4 - 0.75 meters
Rastered Beam Dimensions (Vacuum)	--	:	0.5 - 15 centimeters
Deflector Coil Current	-----	:	4 amperes (Maximum)
Vacuum Chamber Operating Pressure	--	:	~ 10 <sup>-3</sup> torr

Table I: PELLETRON and Raster System Specifications

TABLE II

## BEAM CURRENT DISPOSITION

1.0 MeV Electron Beam Vacuum Environment  
All Currents in Microamperes

FARADAY CUP (FC)	MASK <sup>*</sup> (M)	STOPPER <sup>*</sup> (S)	M + S	$\frac{M + S}{FC}$
0.275	0.196	0.078	0.274	0.99
0.502	0.356	0.152	0.508	1.01
1.02	0.695	0.283	0.978	0.96
1.92	1.29	0.587	1.88	0.98

<sup>\*</sup>Corrected for electron backscatter

Table II: Beam Current Disposition

TABLE III  
 ELECTRON TRANSPORT IN WINDOW MATERIALS  
 Transmitted Electron Angular Distributions  
 0.0254 cm Beryllium

Scattering Angle Degrees	Scattered Electron Fraction	
	E <sub>b</sub> = 0.4 MeV	E <sub>b</sub> = 1.0 MeV
0 - 10	0.076	0.290
10 - 20	0.197	0.447
20 - 30	0.230	0.195
30 - 40	0.198	0.051
40 - 50	0.122	0.014
50 - 60	0.074	-----

0.00254 cm Mylar

Scattering Angle Degrees	Scattered Electron Fraction	
	E <sub>b</sub> = 0.4 MeV	E <sub>b</sub> = 1.0 MeV
0 - 5	0.138	0.470
5 - 10	0.297	0.440
10 - 15	0.298	0.091
15 - 20	0.170	-----
20 - 25	0.073	-----
25 - 30	0.022	-----

Table III: Electron Transport in Window Materials



TABLE IV  
ELECTRON TRANSPORT IN THIN BERYLLIUM AND MYLAR FOILS

Transmitted Electron Angular Distributions

0.00254 cm Mylar

Scattering Angles Degrees	Scattered Electron Fraction	
	$E_b = 0.4$ MeV	$E_b = 1.0$ MeV
0 - 10	0.431	0.902
10 - 20	0.467	0.095
20 - 30	0.095	-----

0.00254 cm Beryllium

Scattering Angle Degrees	Scattered Electron Fraction	
	$E_b = 0.4$ MeV	$E_b = 1.0$ MeV
0 - 10	0.511	0.950
10 - 20	0.427	0.041
20 - 30	0.059	-----

0.00508 cm Beryllium

Scattering Angle Degrees	Scattered Electron Fraction	
	$E_b = 0.4$ MeV	$E_b = 1.0$ MeV
0 - 10	0.394	0.779
10 - 20	0.430	0.215
20 - 30	0.127	-----
30 - 40	0.035	-----

Table IV: Electron Transport in Thin Beryllium and Mylar Foils

DISTRIBUTION:

U.S. NRC Distribution Contractor  
7300 Pearl Street  
Bethesda, MD 20014  
375 copies for RV

Ansaldo Impianti  
Centro Sperimentale del Boschetto  
Corso F.M. Perrone, 118  
16161 Genova  
ITALY  
Attn: C. Bozzolo

Ansaldo Impianti  
Via Gabriele D'Annunzio, 113  
16121 Genova  
ITALY  
Attn: S. Grifoni

ASEA-ATOM  
Department KRD  
Box 53  
S-721 04  
Vasteras  
SWEDEN  
Attn: A. Kjellberg

ASEA-ATOM  
Department TQD  
Box 53  
S-721 04  
Vasteras  
SWEDEN  
Attn: T. Granberg

ASEA KABEL AB  
P.O. Box 42 108  
S-126 12  
Stockholm  
SWEDEN  
Attn: B. Dellby

Atomic Energy of Canada, Ltd.  
Chalk River Nuclear Laboratories  
Chalk River, Ontario K0J 1J0  
CANADA  
Attn: G. F. Lynch

Atomic Energy of Canada, Ltd.  
1600 Dorchester Boulevard West  
Montreal, Quebec H3H 1P9  
CANADA  
Attn: S. Nish

Bhabha Atomic Research Centre  
Health Physics Division  
BARC  
Bombay-85  
INDIA  
Attn: S. K. Mehta

British Nuclear Fuels Ltd.  
Springfields Works  
Salwick, Preston  
Lancs  
ENGLAND  
Attn: W. G. Cunliff, Bldg 334

Brown Boveri Reaktor GMBH  
Postfach 5143  
D-6800 Mannheim 1  
WEST GERMANY  
Attn: R. Schemmel

Bundesanstalt fur Materialprufung  
Unter den Eichen 87  
D-1000 Berlin 45  
WEST GERMANY  
Attn: K. Wundrich

CEA/CEN-FAR  
Departement de Surete Nucleaire  
Service d'Analyse Fonctionnelle  
B.P. 6  
92260 Fontenay-aux-Roses  
FRANCE  
Attn: M. Le Meur  
J. Henry

CERN  
Laboratoire 1  
CH-1211 Geneve 23  
SWITZERLAND  
Attn: H. Schonbacher

Canada Wire and Cable Limited  
Power & Control Products Division  
22 Commercial Road  
Toronto, Ontario  
CANADA M4G 1Z4  
Attn: Z. S. Paniri

Commissariat a l'Energie Atomique  
ORIS/LABRA  
BP N° 21  
91190 Gif-Sur-Yvette  
FRANCE  
Attn: G. Gaussens  
J. Chenion  
F. Carlin

Commissariat a l'Energie Atomique  
CEN Cadarache DRE/STRE  
BP N° 1  
13115 Saint Paul Lez Durance  
FRANCE  
Attn: J. Campan

Conductores Monterrey, S. A.  
P.O. Box 2039  
Monterrey, N. L.  
MEXICO  
Attn: P. G. Murga

Electricite de France  
Direction des Etudes et Recherches  
1, Avenue du General de Gaulle  
92141 CLAMART CEDEX  
FRANCE  
Attn: J. Roubault  
L. Deschamps

Electricite de France  
Direction des Etudes et Recherches  
Les Renardières  
Boite Postale n° 1  
77250 MORET SUR LORING  
FRANCE  
Attn: Ph. Roussarie  
V. Deglon  
J. Ribot

EURATOM  
Commission of European Communities  
C.E.C. J.R.C.  
21020 Ispra (Varese)  
ITALY  
Attn: G. Mancini

FRAMATOME  
Tour Fiat - Cedex 16  
92084 Paris La Defense  
FRANCE  
Attn: G. Chauvin  
E. Raimondo

Furukawa Electric Co., Ltd.  
Hiratsuka Wire Works  
1-9 Higashi Yawata - 5 Chome  
Hiratsuka, Kanagawa Pref  
JAPAN 254  
Attn: E. Oda

Gesellschaft fur Reaktorsicherheit (GRS) mbH  
Glockengasse 2  
D-5000 Koln 1  
WEST GERMANY  
Attn: Library

Gesellschaft fur Reaktorsicherheit (GRS) mbH  
Forschungsgelände  
8046 Garching  
WEST GERMANY  
Attn: S. Gossner

Health & Safety Executive  
Thames House North  
Milbank  
London SW1P 4QJ  
ENGLAND  
Attn: W. W. Ascroft-Hutton

ITT Cannon Electric Canada  
Four Cannon Court  
Whitby, Ontario L1N 5V8  
CANADA  
Attn: B. D. Vallillee

Imatran Voima Oy  
Electrotechn. Department  
P.O. Box 138  
SF-00101 Helsinki 10  
FINLAND  
Attn: B. Regnell  
K. Koskinen

Institute of Radiation Protection  
Department of Reactor Safety  
P.O. Box 268  
00101 Helsinki 10  
FINLAND  
Attn: L. Reiman

Instituto de Desarrollo y Diseno  
Ingar - Santa Fe  
Avellaneda 3657  
C.C. 34B  
3000 Santa Fe  
REPUBLICA ARGENTINA  
Attn: N. Labath

Japan Atomic Energy Research Institute  
Takasaki Radiation Chemistry  
Research Establishment  
Watanuki-machi  
Takasaki, Gunma-ken  
JAPAN

Attn: N. Tamura  
K. Yoshida

Japan Atomic Energy Research Institute  
Tokai-Mura  
Naka-Gun  
Ibaraki-Ken  
319-11  
JAPAN

Attn: Y. Koizumi

Japan Atomic Energy Research Institute  
Osaka Laboratory for Radiation Chemistry  
25-1 Mii-Minami machi,  
Neyagawa-shi  
Osaka 572  
JAPAN

Attn: Y. Nakase

Kraftwerk Union AG  
Department R361  
Hammerbacherstrasse 12 + 14  
D-8524 Erlangen  
WEST GERMANY  
Attn: I. Terry

Kraftwerk Union AG  
Section R541  
Postfach: 1240  
D-8757 Karlstein  
WEST GERMANY  
Attn: W. Siegler

Kraftwerk Union AG  
Hammerbacherstrasse 12 + 14  
Postfach: 3220  
D-8520 Erlangen  
WEST GERMANY  
Attn: W. Morell

Motor Columbus  
Parkstrasse 27  
CH-5401  
Baden  
SWITZERLAND  
Attn: H. Fuchs

NOK AG Baden  
Beznau Nuclear Power Plant  
CH-5312 Doettingen  
SWITZERLAND  
Attn: O. Tatti

Norsk Kabelfabrik  
3000 Drammen  
NORWAY  
Attn: C. T. Jacobsen

Nuclear Power Engineering Test Center  
6-2, Toranomon, 3-Chome  
Minato-ku  
No. 2 Akiyana Building  
Tokyo 105  
JAPAN

Attn: S. Maeda  
Ontario Hydro  
700 University Avenue  
Toronto, Ontario M5G 1X6  
CANADA  
Attn: R. Wong  
B. Kukreti

Oy Stromberg Ab  
Helsinki Works  
Box 118  
FI-00101 Helsinki 10  
FINLAND  
Attn: P. Paloniemi

Rheinisch-Westfallscher  
Technischer Uberwachung-Vereln e.V.  
Postfach 10 32 61  
D-4300 Essen 1  
WEST GERMANY  
Attn: R. Sartori

Sydskraft  
Southern Sweden Power Supply  
21701 Malmo  
SWEDEN  
Attn: O. Grondalen

UKAEA  
Materials Development Division  
Building 47  
AERE Harwell  
OXON OX11 0RA  
ENGLAND  
Attn: D. C. Phillips

United Kingdom Atomic Energy Authority	1200	G. Yonas
Safety & Reliability Directorate	1231	J. A. Halbleib, Jr.
Wigshaw Lane	1234	J. Chang
Culcheth	1234	G. J. Lockwood
Warrington WA3 4NE	1234	L. E. Ruggles
ENGLAND	1800	R. L. Schwoebel
Attn: M. A. H. G. Alderson	1810	R. G. Keplcr
	1811	L. A. Harrah
Waseda University	1811	R. L. Clough
Department of Electrical Engineering	1812	K. T. Gillen
4-1 Ohkubo-3, Shinjuku-ku	1813	J. G. Curro
Tokyo	1815	R. T. Johnson
JAPAN	2155	J. E. Gover
Attn: K. Yahagi	2155	O. M. Stuetzer
	2321	D. McKeon
	2341	M. B. Murphy
	5200	W. C. Myre
	6200	V. L. Dugan
	6300	R. W. Lynch
	6400	A. W. Snyder
	6410	J. W. Hickman
	6420	J. V. Walker
	6432	D. D. Carlson
	6440	D. A. Dahlgren
	6442	W. A. Von Riesemann
	6444	S. L. Thompson
	6445	B. E. Bader
	6445	P. R. Bennett
	6445	L. D. Bustard
	6445	C. M. Craft
	6446	L. L. Bonzon (20)
	6446	W. H. Buckalew
	6446	J. W. Grossman
	6446	D. B. Hente
	6446	S. M. Luker
	6446	F. V. Thome
	6446	F. J. Wyant
	6447	D. L. Berry
	6449	K. D. Bergeron
	6450	J. A. Reuscher
	6450A	J. Bryson
	6452	M. Aker/J. S. Philbin
	8424	M. A. Pound
	3141-1	C. M. Ostrander (5)
	3151	W. L. Garner

**BIBLIOGRAPHIC DATA SHEET**

NUREG/CR-3777  
SAND84-0912

3 TITLE AND SUBTITLE

Capabilities and Diagnostics of the Sandia  
Pelletron-Raster System

6 AUTHOR(S)

W. H. Buckalew, G. J. Lockwood, S. M. Luker,  
L. E. Ruggles, E. J. Wyant

8 PERFORMING ORGANIZATION NAME AND MAILING ADDRESS (Include Zip Code)

Sandia National Laboratories  
Albuquerque, New Mexico 87185

11 SPONSORING ORGANIZATION NAME AND MAILING ADDRESS (Include Zip Code)

Electrical Engineering Branch  
Division of Engineering Technology  
Office of Nuclear Regulatory Research  
U. S. Nuclear Regulatory Commission  
Washington, DC 20555

13 SUPPLEMENTARY NOTES

14 ABSTRACT (200 words or less)

The radiation capabilities of the PELLETRON Electron Beam Accelerator have been expanded to include a controllable, variable dimension, beam diffusion option. This rastered beam option has been studied in detail. Beam characteristics have been determined as a function of incident electron beam energy, current, and deflection system parameters. The beam diagnostics required to define any given diffuse beam pattern are accurate and predictable. Recently, utility of this added PELLETRON capability was demonstrated by simulating the effects of complex nuclear reactor accident electron environments on electrical insulation materials similar to those used in nuclear power plants.

15a KEY WORDS AND DOCUMENT ANALYSIS

15b DESCRIPTORS

16 AVAILABILITY STATEMENT

Unlimited

17 SECURITY CLASSIFICATION  
(This report)

Unclassified

19 SECURITY CLASSIFICATION  
(This page)

Unclassified

18 NUMBER OF PAGES

53

20 PRICE

\$

7 LITERATURE

4 RECIPIENT'S ACCESSION NUMBER

5 DATE REPORT COMPLETED

MONTH YEAR  
May 1984

7 DATE REPORT ISSUED

MONTH YEAR  
June 1984

9 PROJECT TASK WORK UNIT NUMBER

10 FIN NUMBER

NRC FIN No. A-1051

12a TYPE OF REPORT

12b PERIOD COVERED (Inclusive dates)

120555078877 1 IANIRV  
US NRC  
ADM-DIV OF TIDC  
POLICY & PUB MGT BR-PDR NUREG  
W-501 DC 20555  
WASHINGTON